



Inter-comparison of MAX-DOAS measurements of tropospheric HONO slant column densities and vertical profiles during the CINDI-2 Campaign

- 5 Yang Wang¹, Arnoud Apituley², Alkiviadis Bais³, Steffen Beirle¹, Nuria Benavent⁴, Alexander Borovski⁵, Ilya Bruchkouski⁶, Ka Lok Chan^{7, 8}, Sebastian Donner¹, Theano Drosoglou³, Henning Finkenzeller^{9, 10}, Martina M. Friedrich¹¹, Udo Frieb¹², David Garcia-Nieto⁴, Laura Gómez-Martín¹³, François Hendrick¹¹, Andreas Hilboll¹⁴, Junli Jin¹⁵, Paul Johnston¹⁶, Theodore K. Koenig^{9, 10}, Karin Kreher¹⁷, Vinod Kumar¹, Aleksandra Kyuberis¹⁸, Johannes Lampel^{12, 19}, Cheng Liu²⁰, Haoran Liu²⁰,
10 Jianzhong Ma²¹, Oleg L. Polyansky^{22,18}, Oleg Postlyakov⁵, Richard Querel¹⁶, Alfonso Saiz-Lopez⁴, Stefan Schmitt¹², Xin Tian^{23, 24}, Jan-Lukas Tirpitz¹², Michel Van Roozendael¹¹, Rainer Volkamer^{9, 10}, Zhuoru Wang⁸, Pinhua Xie²⁴, Chengzhi Xing²⁵, Jin Xu²⁴, Margarita Yela¹³, Chengxin Zhang²⁵, Thomas Wagner¹

- ¹ Max Planck Institute for Chemistry, Mainz, Germany
15 ² Royal Netherlands Meteorological Institute (KNMI), De Bilt, The Netherlands
³ Laboratory of Atmospheric Physics, Aristotle University of Thessaloniki, Thessaloniki, Greece
⁴ Department of Atmospheric Chemistry and Climate, Institute of Physical Chemistry Rocasolano (CSIC), Madrid, Spain
⁵ A. M. Obukhov Institute of Atmospheric Physics, Russian Academy of Sciences, Moscow, Russia
⁶ National Ozone Monitoring Research and Education Center BSU (NOMREC BSU), Belarusian State University, Minsk,
20 Belarus
⁷ Meteorologisches Institut, Ludwig-Maximilians-Universität München, Munich, Germany
⁸ Remote Sensing Technology Institute, German Aerospace Center (DLR), Oberpfaffenhofen, Germany
⁹ Department of Chemistry, University of Colorado Boulder, Boulder, CO, USA
¹⁰ Cooperative Institute for Research in Environmental Sciences, Boulder, CO, USA
25 ¹¹ Royal Belgian Institute for Space Aeronomy, Brussels, Belgium
¹² Institute of Environmental Physics, University of Heidelberg, Heidelberg, Germany
¹³ National Institute of Aerospace Technology, Madrid, Spain
¹⁴ Institute of Environmental Physics, University of Bremen, Bremen, Germany
¹⁵ Meteorological Observation Center, China Meteorological Administration, Beijing, China
30 ¹⁶ National Institute of Water & Atmospheric Research (NIWA), Lauder, New Zealand
¹⁷ BK Scientific, Mainz, Germany
¹⁸ Institute of Applied Physics, Russian Academy of Sciences, Nizhny Novgorod, Russia
¹⁹ Airyx GmbH, Justus-von-Liebig-Str. 14, 69214 Eppelheim, Germany
²⁰ Department of Precision Machinery and Precision Instrumentation, University of Science and Technology of China, Hefei,
35 Anhui, China
²¹ Chinese Academy of Meteorology Science, China Meteorological Administration, Beijing, China
²² Department of Physics and Astronomy, University College London, Gower St, London WC1E 6BT, UK
²³ Institutes of Physical Science and Information Technology, Anhui University, Hefei, 230601, China
²⁴ Anhui Institute of Optics and Fine Mechanics, Chinese Academy of Sciences, Hefei, China
40 ²⁵ School of Earth and Space Sciences, University of Science and Technology of China, Hefei, Anhui, China

Correspondence to: Yang Wang (y.wang@mpic.de)

45 Abstract.

We present the inter-comparison of delta slant column densities (SCDs) and vertical profiles of nitrous acid (HONO) derived from measurements of different MAX-DOAS instruments and using different inversion algorithms during the Second Cabauw Inter-comparison campaign for Nitrogen Dioxide measuring Instruments (CINDI-2), in September 2016, at Cabauw, The Netherlands (51.97° N, 4.93° E). Systematic discrepancies of HONO delta SCDs are observed in the range of ±
50 0.3×10^{15} molecules cm^{-2} , which is half of the typical random discrepancy of 0.6×10^{15} molecules cm^{-2} . For a typical high HONO delta SCD of 2×10^{15} molecules cm^{-2} , the relative systematic and random discrepancies are about 15% and 30%, respectively. The inter-comparison of HONO profiles shows that both systematic and random discrepancies of HONO VCDs and near-surface volume mixing ratios (VMRs) are mostly in the range of $\sim \pm 0.5 \times 10^{15}$ molecules cm^{-2} and $\sim \pm 0.1$ ppb



(typically ~ 20%). Further we find that the discrepancies of the retrieved HONO profiles are dominated by discrepancies of the HONO delta SCDs. The profile retrievals only contribute to the discrepancies of the HONO profiles by ~5%. However, some data sets with substantial larger discrepancies than the typical values indicate that inappropriate implementations of profile inversion algorithms and configurations of radiative transfer models in the profile retrievals can also be an important uncertainty source. In addition, estimations of measurement uncertainties of HONO dSCDs, which can significantly impact profile retrievals using the optimal estimation method, need to consider not only DOAS fit errors, but also atmospheric variability, especially for an instrument with a DOAS fit error lower than $\sim 3 \times 10^{15}$ molecules cm^{-2} . The MAX-DOAS results during the CINDI-2 campaign indicate that the peak HONO levels (e.g. near-surface VMRs of ~ 0.4 ppb) often appeared in the early morning and below 0.2 km. The near-surface VMRs retrieved from the MAX-DOAS observations are compared with those measured using a co-located long-path DOAS instrument. The systematic differences are smaller than 0.15 ppb and 0.07 ppb during early morning and around noon, respectively. Since true HONO values at high altitudes are not known in the absence of real measurements, in order to evaluate the abilities of profile inversion algorithms to respond to different HONO profile shapes, we performed sensitivity studies using synthetic HONO delta SCDs simulated by a radiative transfer model with assumed HONO profiles. The tests indicate that the profile inversion algorithms based on the optimal estimation method with proper configurations can well reproduce the different HONO profile shapes. Therefore we conclude that the feature of HONO accumulated near the surface derived from MAX-DOAS measurements are expected to well represent the ambient HONO profiles.

1 Introduction

Multi Axis - Differential Optical Absorption Spectroscopy (MAX-DOAS) is widely used as a ground-based remote sensing technique for retrieving lower tropospheric vertical profiles of trace gases (e.g. NO_2 , SO_2 , HCHO, etc.) and aerosols from sequential measurements of ultraviolet and visible spectra of scattered sunlight recorded at multiple elevation angles (Hönninger and Platt, 2002; Bobrowski et al., 2003; Van Roozendael et al., 2003; Hönninger et al., 2004; Wagner et al., 2004 and Wittrock et al., 2004). MAX-DOAS instruments have been developed with different optical and mechanical systems by different research groups and companies in order to meet the requirements of high accuracy and automatic operation. MAX-DOAS measurements have been widely used, especially for the validation of satellite products (e.g. Ma et al., 2013; Kanaya et al., 2014; Jin et al., 2016a; Wang et al., 2017a; Liu et al., 2019). Inversion procedures of MAX-DOAS measurements normally contain two steps: 1) spectral analysis to derive tropospheric differential slant column densities (delta SCDs) of trace gases; 2) retrieval of vertical profiles from the dependencies of the delta SCDs on elevation angle. Note that the definitions of SCD, dSCD, and delta SCD are given in section 2.2.1. Different programs, e.g. QDOAS (Danckaert et al., 2017), WINDOAS (Fayt and van Roozendael, 2009) and DOASIS (Kraus et al., 2006), have been developed for the spectral analysis based on the DOAS technique (Platt and Stutz, 2008, and references therein). The spectral analysis can strongly depend on the configuration of fit parameters, e.g. wavelength ranges, cross sections, polynomials, and intensity offset corrections. Inversion algorithms of vertical profiles of trace gases and aerosols have been developed in previous studies based on the optimal estimation (OE) method (Rodgers, 2000; Frieß et al., 2006, 2011; Wittrock, 2006; Irie et al., 2008, 2011; Clémer et al., 2010; Yilmaz, 2012; Hartl and Wenig, 2013; Wang Y. et al., 2013a, b, 2017b; Chan et al., 2018; Bösch et al., 2018) and parameterised approaches (Li et al., 2010, 2013; Vlemmix et al., 2010, 2011, 2015; Wagner et al., 2011; Beirle et al., 2018), respectively. Both types of retrievals require radiative transfer model (RTM) simulations to calculate air mass factors (AMF). These algorithms utilise different iterative approaches, different software implementations, and different RTM. For inversion algorithms based on the OE method, retrieval results can be significantly affected by the choices of the a priori constraints, e.g. a priori profiles, covariance of uncertainties, and aerosol optical properties. For parameterised approaches, only the profile scenarios which are considered for building the look-up-table can be retrieved



95 from real measurements. Like for the profiles retrieved by OE, the retrieved profiles can be considerably impacted by the
assumed profile parameters, aerosol optical properties, or fit and profile selection approaches. In order to generate
harmonized data sets from worldwide MAX-DOAS observations, it is necessary to evaluate the consistency of MAX-DOAS
results derived from measurements of different MAX-DOAS instruments and using different programs for spectral analysis
and profile inversion. For this purpose, a series of campaigns, including the Cabauw Inter-comparison campaign of Nitrogen
100 Dioxide measuring Instruments (CINDI) in The Netherlands in June–July 2009 (<http://projects.knmi.nl/cindi/>, Piters et al.,
2012), the Multi Axis DOAS – Comparison campaign for Aerosols and Trace gases (MAD-CAT) in Germany in June and
July 2013 (http://joseba.mpch-mainz.mpg.de/mad_cat.htm), and the CINDI-2 campaign in The Netherlands in September
2016 (<http://www.tropomi.eu/data-products/cindi-2>, Apituley et al. 2019) were organized. 36 MAX-DOAS instruments
designed and operated by 24 different institutes across the world participated in the CINDI-2 campaign. In previous studies,
105 SCDs of NO₂, HCHO, O₃, O₄, retrieved from different instruments have been inter-compared. (e.g. Roscoe et al., 2010;
Pinardi et al., 2013; Zieger et al., 2011; Irie et al., 2011; Friess et al., 2016; Wang et al., 2017c; Peters et al., 2017). Wang et
al. (2017c) presents inter-comparisons of SCDs of nitrous acid (HONO), which has ~10 times lower absorption signals than
NO₂, during the MAD-CAT campaign. Further studies compared profile results of aerosol extinction and NO₂ and HCHO
concentrations retrieved from different instruments and by different inversion algorithms (Frieß et al., 2016; Frieß et al.,
110 2019 and Tirpitz et al., 2020). In this study we focus on the inter-comparison of HONO results (dSCDs and profiles) derived
from MAX-DOAS measurements during the recent CINDI-2 campaign.

In the past decade, several studies have been performed investigating the daytime sources of HONO to unravel their
potential contributions to the OH radical concentration and the tropospheric oxidation capacity (Alicke et al., 2003;
Kleffmann et al., 2005; Acker et al., 2006; Monks et al., 2009; Elshorbany et al., 2010). The gas-phase reaction of NO with
115 the OH radical (Stuhl and Niki, 1972 and Pagsberg et al., 1997) mostly determines the daytime HONO concentration.
However, field measurements (Neftel et al., 1996; Kleffmann et al., 2005; Sörgel et al., 2011; Li et al., 2012 and 2014 and
Wong et al., 2012) and laboratory studies (Akimoto et al., 1987; Rohrer et al., 2005) reported that the well-known gas-phase
reactions can often not explain the observed high daytime concentrations of HONO. To explain this discrepancy, several
suggestions were made: heterogeneous reactions on various surfaces such as the ground, forests, buildings, and aerosols (e.g.
120 Su et al., 2008 and 2011; Li et al., 2014; and references therein), emissions from soil (e.g. Su et al., 2011 and references
therein), and a potential gas-phase reaction between HO_x and NO_x (Li et al., 2014). Since vertical profiles of HONO can
indicate the height of the dominant HONO sources, MAX-DOAS measurements of HONO have drawn major attentions in
recent years. However, HONO retrievals from MAX-DOAS measurements are still challenging due to typically low HONO
volume mixing ratios (VMRs) of <1 ppb (corresponding to a typical optical depth of <0.005) even in polluted regions.
125 Although several studies have reported HONO profile retrievals using MAX-DOAS measurements at different locations (e.g.
Hendrick et al., 2014; Ryan et al., 2018; Wang et al., 2018a), so far few efforts have been made to study the consistency of
HONO results, especially the vertical profiles, retrieved from different MAX-DOAS instruments and using different
inversion algorithms. In our previous study (Wang et al., 2017c) based on measurements made during the MAD-CAT
campaign, we evaluated discrepancies of HONO SCDs between seven MAX-DOAS instruments, quantified error sources of
130 the DOAS fits, and concluded on recommended DOAS fit parameters based on sensitivity studies. In this study, we extend
the HONO inter-comparison activity to more MAX-DOAS instruments and include also the comparison of the HONO
vertical profiles retrieved during the CINDI-2 campaign. Furthermore, we evaluate the dependence of the retrieved HONO
profiles on different shapes and discuss the optimal a priori settings based on synthetic studies using RTM simulations. The
effects of varying vertical grid intervals on the profile retrievals are also discussed based on sensitivity tests.

135 This paper is structured as follows. Section 2 provides an overview of the CINDI-2 campaign, comparison schemes of HONO
delta SCD and profile results, the RTM simulations for the analysis of synthetic spectra, and cloud classifications introduced
for the inter-comparisons. Section 3 and 4 present inter-comparison results of HONO delta SCDs and profiles, respectively,



derived from real measurements by the participating instruments. The sensitivity studies of HONO profile inversions based on synthetic analysis are given in Section 5. The conclusions are presented in Section 6.

140 **2 CINDI-2 Inter-comparison campaign**

2.1 CINDI-2 campaign and HONO inter-comparison activities

The CINDI-2 campaign was held in the period from 12 to 28 September 2016, at the remote-sensing site of the CESAR station (51.971° N, 4.927° E) (<http://www.cesar-observatory.nl/>) in a rural area in Cabauw, the Netherlands. The measurement site is surrounded by pasture and farmland, and is located ~20 km southwest of the city of Utrecht and ~30 km east of the city of Rotterdam. 36 MAX-DOAS instruments participated in the campaign and were operated by different research groups. Different optical, electrical and mechanical systems with different spectrometers were used in the different MAX-DOAS instruments. In order to optimize the synchronisation of the measurements for the inter-comparisons, all MAX-DOAS instruments were installed close to each other and measured following a consistent protocol (see <http://www.tropomi.eu/data-products/planning-information>). Some instruments measure also at different azimuth angles and are categorized in the following as 2D systems, whereas others can only measure at one fixed azimuth angle and are categorized as 1D systems. Because of these differences, 2D systems and 1D systems followed different measurement protocols. 1D systems continuously measured at the fixed azimuth direction of 287° with four elevation sequences in each hour. 2D systems routinely measured at 7 different azimuth angles in each hour, and in the time slot of 15 minutes at the beginning of each hour at the same azimuth angle (287°) as the 1D systems. Therefore in the first 15 minutes of each hour, all instruments measure at the same azimuth angle of 287° and used the same elevation sequence of 1, 2, 3, 4, 5, 6, 8, 15, 30 and 90°. The same integration time of one min for individual measurements was applied by all instruments.

Further information about the campaign and the participating instruments can be found in Apituley et al. (2019) and Kreher et al. (2019). So far CINDI-2 data have been used in Donner et al. (2019) for the study on the accuracy of different elevation calibration methods, in Kreher et al., 2019 for carrying out a semi-blind inter-comparison of NO₂, O₄, O₃ and HCHO slant column densities, and in Frieß et al. (2019) and Tirpitz et al. (2020) for the study of the consistency of profile retrievals of aerosols, NO₂, and HCHO derived from different inversion programs and instruments based on synthetic and measured spectra. Additionally, the CINDI-2 data were used by Wang et al. (2018b) to develop new retrieval algorithms for tropospheric ozone profiles and by Beirle et al. (2019) for demonstrating the performance of MAPA profile inversion algorithm.

13 MAX-DOAS instruments operated by different researchers joined this study on the retrievals of tropospheric HONO. An overview of the participants, their instruments and analysis tools is provided in Table 1. The comparison activities were performed in two steps. First, the consistency of the HONO delta SCDs was evaluated and then an inter-comparison of the derived vertical profiles was performed. The details of the retrieval settings, comparison schemes, and participating instruments and algorithms are given in section 2.2 and 2.3, respectively.

170 **2.2 Inter-comparison of tropospheric HONO slant column densities**

2.2.1 Baseline retrieval settings and comparison schemes

Baseline DOAS retrieval settings were selected decided based on the recommended settings from a previous study during the MAD-CAT campaign (Wang et al., 2017c). The parameters of the baseline settings are given in Table 2. Different participants applied the baseline settings using different DOAS fit programs independent from each other. Absorption cross sections of HONO, NO₂, O₃, BrO, O₄, HCHO, and H₂O were convolved with the slit function of the individual instruments before being included in DOAS fits. The slant column density (SCD) represents the trace gas concentration integrated along the light path. Differential SCDs (dSCDs) are the direct output from a DOAS fit of a measured spectrum and represent the



180 difference of the SCDs in a measured spectrum and a Fraunhofer reference spectrum. The Fraunhofer reference spectrum is usually measured at the elevation angle of 90° in order to acquire the shortest light path in the troposphere. If both the measured off-zenith spectrum and the Fraunhofer reference spectrum in a DOAS fit are recorded at approximately the same solar zenith angle (SZA), the retrieved dSCD only contains the absorptions along the light path in the troposphere, since both measurements have almost the same stratospheric light path. Therefore, in such cases, the retrieved dSCD directly represents the tropospheric SCD. In the pioneering study of Hönninger et al. (2004), it is referred to as delta SCD. Since delta SCDs are normally used in the retrievals of tropospheric vertical profiles, we first inter-compare the HONO delta SCDs between the different instruments. There are two procedures to retrieve delta SCDs from off-zenith MAX-DOAS measurements, which use two different Fraunhofer reference spectra (FRS), namely the so-called “sequential FRS” and “daily noon FRS”. The “sequential FRS” is derived from interpolation of two spectra measured in zenith view before and after an elevation sequence to match the time of the off-zenith measurements. The “daily noon FRS” is obtained from the mean of all zenith-sky spectra acquired between 11:30:00 and 11:41:00 UTC on individual days. The differential SCDs retrieved using the “sequential FRS” can directly be regarded as the delta SCDs. In contrast, a post-processing is needed to convert the differential SCDs (dSCDs) retrieved using the “daily noon FRS” into delta SCDs. For individual HONO dSCDs retrieved from off-zenith measurements, a reference dSCD can be derived by a time-interpolation of the HONO dSCDs retrieved from zenith measurements before and after the off-zenith measurement. The HONO delta SCDs is then derived by subtracting this reference dSCD from the corresponding off-zenith dSCDs. The mathematic derivation of delta dSCDs with the two procedures has been discussed in section 3.1 of Wang et al. (2017c). Although the “sequential” FRS can compensate for the effects of instability of instrumental properties on DOAS retrievals, the “daily noon FRS” is easier to be implemented in typical DOAS programs than the “sequential FRS”. Therefore the “daily noon FRS” was often used in previous studies. In this study, comparison activities of HONO delta SCDs are separated into two parts: for retrievals using either the “sequential FRS” or the “daily noon FRS”, the results of the different instruments are compared. Additionally, for individual instruments, the HONO delta SCDs retrieved using the two different FRS are also compared in order to quantify the potential bias of the HONO retrievals due to the different FRS procedures.

2.2.2 Participating instruments

205 The institutes and instruments participating to the SCD inter-comparison activities are listed in Table 1. It should be noted that “USTC (1)” and “USTC (2)” represent two data sets derived from two MAX-DOAS instruments operated by the “USTC” researchers. Additionally, the spectra recorded by the two “USTC” instruments are independently analysed by the “DLR” researchers, which are marked as “DLR (1)” and “DLR (2)”. Considering the different measurement protocols followed by the 2D system and 1D system instruments, only coincident measurements in the first 15 minutes of each hour are included in the inter-comparison activities. The participating instruments are separated into three groups, consisting of in-house developed instruments by individual groups, EnviMes instruments developed at the University of Heidelberg (Lampel et al., 2015) and recently commercialised (<http://www.airyx.de>), and Mini-DOAS instruments produced in Germany by Hoffmann GmbH (<http://www.hmm.de/>).

2.3 Inter-comparisons of tropospheric HONO profiles

2.3.1 Baseline retrieval settings and inversion algorithms

215 HONO profiles are retrieved from the elevation angle dependency of the HONO delta SCDs using inversion algorithms. Five inversion algorithms based on the optimal estimation (OE) method are used in this study: PriAM (Wang Y. et al., 2013a, b, 2017b), BePro (Clémer et al., 2010), MMF (Friedrich et al., 2019), HEIPRO (Frieß et al., 2006, 2011), and M³ (Chan et al., 2018). Different from the other algorithms, MAPA (Beirle et al., 2019) implemented by the “MPIC” participants is based on a profile parameterization. The corresponding algorithms implemented by individual participants are listed in Table 1. Note



that PriAM, BePro, and HEIPRO are independently implemented by several participants. Some parameters are harmonized
220 between the different inversion algorithms. Information on these parameters and on the atmospheric properties used in the
RTM is summarised in Table 3. Note that no assumptions on the measurement uncertainty covariance, a priori profiles, and a
priori covariance matrices are made in MAPA. The wavelength of the RTM simulations of the HONO AMFs for the profile
retrievals is 355 nm, representing the effective wavelength of the HONO absorption in the spectral range of DOAS fits of
HONO delta SCDs. The effective wavelength is calculated by weighting the wavelengths by the HONO cross section values
225 in the spectral range of 335-373 nm of the HONO DOAS fits. The atmospheric properties and aerosol properties are set based
on typical conditions near the measurement site during the CINDI-2 campaign period. Profiles are retrieved in the altitude
range of 0 to 4 km with a grid of 200 m. Vertical profiles of aerosol extinction are required as an input for the HONO profile
retrievals, and were retrieved around 360nm from O₃ delta SCDs, which are retrieved from the MAX-DOAS measurements
in the spectral range of 338 – 370 nm. The details of the aerosol retrievals can be found in Tirpitz et al., 2020. Following
230 previous studies (e.g. Hendrick et al., 2014 and Wang et al., 2018), the covariance of the measurement uncertainties is set to
square of 100% of the DOAS fit error of the HONO dSCDs for the diagonal elements and zero for the extra-diagonal
elements. The a priori profile is arbitrarily set as an exponentially-decreasing profile with a VCD of 3×10^{14} molecules cm⁻²
and a scaling height (SH) of 0.1 km. The selection of the a priori profile shape is based on the fact that HONO is typically
accumulated at altitudes close to the surface (Hendrick et al., 2014 and Wang et al., 2018). Similar to measurement
235 uncertainties, and following the previous studies (e.g., Hendrick et al., 2014 and Wang et al., 2018), the covariance of the a
priori profile (S_a) is set to square of 100% of a priori values for the diagonal elements. The extra-diagonal elements are
calculated using a Gaussian function based on the neighbouring diagonal elements with a correlation length of 200 m.
For the algorithms based on the optimal estimation method, each of them used different RTMs as forward model and applied
different iterative procedures. PriAM and HEIPRO use the RTM SCIATRAN version 2 (Rozanov et al., 2005). BePro, MMF,
240 and M³ use the RTM LIDORT (Spurr et al., 2008), VLIDORT (Spurr et al., 2013), and LibRadTran (Mayer and Kylling,
2005; Emde et al., 2016), respectively. Another important difference is that in order to avoid negative concentrations of the
retrieved results (which are not possible in the real atmosphere), the retrievals are done in logarithmic space (see details in
Yilmaz, 2012) by PriAM, HEIPRO, and MMF. Since distribution probabilities of retrieved profiles around a priori profiles
become asymmetric due to the inversion in the logarithm space, the sensitivity of the inversion to large values is larger than
245 that in the linear space. A nonlinear iterative procedure is applied for the inversion of both aerosol and trace gas profiles in
PriAM, HEIPRO, and MMF, whereas a linear iterative procedure is adapted for trace gas retrievals in the other two
algorithms.

2.3.2 Comparison scheme

In order to attribute the discrepancies between the different data sets of HONO profiles to different possible causes
250 (instrumental properties, FRS selection, profile inversion algorithms, and aerosol inversions), the inter-comparison of the
HONO profiles are subdivided into four tasks named T1a, T1b, T2a, and T2b. In all four tasks, the HONO profiles are
retrieved using different inversion algorithms by individual participants, while the differences between the tasks are the
choices of the input HONO delta SCDs and aerosol profiles.

In tasks T1a and T1b, the input HONO delta SCDs are those retrieved from measurements of the individual instruments by
255 the individual participants. Differently, in tasks T2a, and T2b, different participants use the same HONO delta SCDs, which
are retrieved from measurements of the “MPIC” instrument by “MPIC”. Using different input delta SCDs allows
investigating whether the discrepancies of the HONO profiles are related to differences of HONO delta SCD retrievals or the
profile inversion algorithms, respectively. For the tasks T1a and T1b either the “sequential FRS” or the “daily noon FRS”
were used in the DOAS fits, respectively, which allows to quantify the effect of the FRS selections on the HONO profile
260 retrievals. The tasks T2a and T2b differ with regard to the input profiles of aerosol extinction used for HONO profile



inversion. In task T2a, different participants used the same aerosol profiles, which are retrieved from the O₄ delta SCDs derived from the “MPIC” MAX-DOAS measurements using the “PriAM” algorithm by “MPIC”. However, in task T2b, the input aerosols are retrieved from the O₄ delta SCDs, derived from the individual MAX-DOAS instruments by the respective participants. Using different input aerosol profiles allows quantifying the effects of aerosol retrievals on the consistency of the HONO profile retrievals. It should be noted that, the input profiles of aerosol extinctions in the tasks T1a and T1b are derived from the aerosol profile retrievals at 340nm, given in Tirpitz et al., 2020, using the common setting by individual participants. In addition, since different measurement protocols are followed by 2D systems and 1D systems (see section 2.2.2), only the coincident HONO measurements in the first 15 minutes of each hour are included in the comparison activities.

2.3.3 Long-Path DOAS measurements for comparisons with MAX-DOAS results

A co-located Long-Path (LP-) DOAS instrument measured HONO concentrations near the surface using an artificial light source during the campaign. The telescope of the LP-DOAS was installed west of the measurement site at a distance of 3800 m. A detailed description of the instrumental set-up can be found elsewhere (Nasse et al., 2019). Four retro-reflector arrays were mounted at different heights (15, 45, 105 and 205 m) at the Cabauw meteorological measurement tower close to the MAX-DOAS site. Consecutive measurements were performed on each retro-reflector leading to a time resolution of approximately 15 minutes. The measurements with the retro-reflector at the height of 205 m result in average HONO concentrations along the light path, which are compared with HONO concentrations in the lowest 200 m layer of profiles derived from MAX-DOAS measurements in section 4.2.2 and 4.3.3. The DOAS fit settings for the retrievals of HONO are given in Table 4.

2.3.4 Synthetic dSCDs for sensitivity analysis

In most of the cases, the true HONO profiles are not known for real MAX-DOAS measurements, which makes it difficult to quantify biases of retrieved HONO profiles with respect to reality. In order to overcome this limitation, we generated a set of synthetic HONO delta SCD using the RTM SCIATRAN, version 3.6.0 (03 Dec 2015) (Rozanov et al., 2014) assuming three different HONO profiles shown in Fig. 1a. The three HONO profiles represent scenarios with HONO accumulated near the surface (profile 1), linearly decreasing with altitude from the surface up to 0.8 km (profile 2), and a box shape profile with constant HONO VMRs in the altitude range from the surface up to 0.8 km and exponentially decreasing to zero above (profile 3). The HONO delta SCDs are simulated by the RTM at 355nm, according to the effective wavelength of HONO DOAS fits in a pseudo-spherical atmosphere with pure Rayleigh scattering (no clouds and aerosols) and with typical temperature and pressure profiles during the campaign. HONO is the only absorber included in the simulations, and the observation geometry is set according to the real measurements on September 14, 2016, during CINDI-2 campaign. In order to test the effect of the measurement noise, we generated a modified data set by adding artificial random noise to the HONO delta SCDs simulated by the RTM with a signal to noise ratio of 3000, which was determined based on the typical noise level of most of the MAX-DOAS instruments in the study. One hundred HONO delta SCDs were generated by adding noise to the individual simulated HONO delta SCDs. This modified data set of HONO delta SCDs with artificial noise is referred to as “noisy synthetic HONO delta SCDs” in the following (see section 5.1). All the synthetic HONO delta SCDs are used in the sensitivity studies presented in section 5.1. The profiles shown in Fig. 1b are used as a priori profiles in the sensitivity studies.

2.4 Cloud classification

In order to evaluate the cloud effects on the MAX-DOAS results and their consistency, the cloud classification scheme described in Wang et al. (2015) and Wagner et al. (2014 and 2016) was applied to the MPIC MAX-DOAS measurements



during the whole CINDI-2 campaign. The sky conditions are identified from the color index (ratio of intensities at 330 nm and 390 nm) and the O₄ dSCDs (retrieved in the spectral range of 338 nm - 370 nm) derived from MAX-DOAS measurements of individual elevation sequences. From the classification scheme, six categories are identified including a) 'cloud free and low aerosol load', b) 'cloud free and high aerosol load', c) 'cloud holes', d) 'broken clouds', e) 'continuous clouds', and f) 'optically thick clouds'. Here, the difference between categories c) and d) is given by the general optical thickness, it is larger for "broken clouds" than for "cloud holes". In order to simplify the comparison activities, the categories of 'cloud free and low aerosol load' and 'cloud free and high aerosol load' are combined and treated as 'clear sky' in this study. The remaining categories, except 'optically thick clouds', are treated as "cloudy sky". It should be noted that the results for the category 'optically thick clouds' are not included in the comparisons because the HONO retrieval quantity is usually strongly degraded for such conditions (Wang et al. 2017b).

3. Results of inter-comparison of tropospheric HONO dSCDs

In this section we present the inter-comparison of HONO delta SCDs derived by the individual participants from their MAX-DOAS measurements using the baseline settings of the DOAS fits (see section 2.2). The overview of the results of the HONO delta SCDs are presented in section 3.1. The overall statistics of the inter-comparisons and the comparison results for the individual participants are discussed in sections 3.1 and 3.2, respectively.

3.1 Overview of tropospheric HONO delta SCDs during the CINDI-2 campaign

For the comparison of the HONO delta SCDs, median values are calculated from the HONO delta SCDs derived from all participants for individual elevation angles separately for the HONO delta SCDs retrieved using the "sequential FRS" and the "daily noon FRS", respectively. The time series of median delta SCDs using the "sequential FRS" are shown in the top panel of Fig. 2a for the time interval of 6 to 17 UTC on the individual days of the campaign. The corresponding sky conditions identified from the MPIC MAX-DOAS measurements (see 2.4) are given in the bottom panel of Fig. 2a. The sky condition results indicate that the frequencies of the "clear sky" and "cloudy sky" conditions are almost equal during the whole campaign. The peak values of the HONO delta SCDs typically appear in the early morning, except September 27, when the peak value of $\sim 3 \times 10^{15}$ molecules cm⁻² is found between 8 to 10 UTC. The peak values in the early morning reach values up to $\sim 8 \times 10^{15}$ molecules cm⁻², as e.g. observed on 21 and 22 September. A large spread of HONO delta SCDs along the elevation angles can be seen and usually with maximum values typically at 1° elevation angle.

3.2 Statistical inter-comparisons of HONO delta SCDs

For the results using the "sequential FRS", median diurnal variations for individual elevation angles of all data sets from all participants are calculated and shown in Fig. 2b. Note that the median values are calculated over both measurement time and all instruments. HONO delta SCDs strongly decrease with increasing elevation angles, especially in the morning, and the spread of the HONO delta SCDs along elevation angles decrease steeply during the day. At 6 UTC the HONO delta SCDs are $\sim 3.2 \times 10^{15}$ molecules cm⁻² and $\sim 0.2 \times 10^{15}$ molecules cm⁻² for elevation angles of 1° and 30°, respectively. During the day, a continuous decrease of the HONO delta SCDs for elevation angles of 1° is seen with the strongest decrease from $\sim 3.2 \times 10^{15}$ to $\sim 1.2 \times 10^{15}$ molecules cm⁻² between 6-8 UTC. For the high elevation angles, the change is much smaller. For instance, the HONO delta SCDs are $\sim 0.2 \times 10^{15}$ molecules cm⁻² at the elevation angles of 30° during the whole day.

In order to evaluate the agreement of the HONO delta SCDs between the different participants, for the same data sets, the diurnal variation of the standard deviation of all HONO delta SCDs compared to the median values is calculated and shown in Fig. 2c. Note that the standard deviations are calculated over both measurement time and all instruments. The standard deviation is much larger in the early morning ($\sim 1.2 \times 10^{15}$ molecules cm⁻²) at 6 UTC than those at a later time. The standard



340 deviations are slightly larger at low elevation angles than those at high elevation angles. Compared to the median values of
the HONO delta SCDs, the relative standard deviation is much smaller at low elevation angles (e.g. 40-100% at 1° elevation
angle) than at high elevation angles (e.g. 200%-400% at 30° elevation angle). Similarly, the relative standard deviation in the
afternoon is much larger than that in the early morning, e.g. 40% at 6 UTC and 100% at 15 UTC, consistent with lower
daytime HONO concentrations (and thus larger relative measurement errors) at the measurement site. Since the DOAS fit
errors indicate the uncertainties of the DOAS retrieval of the HONO delta SCDs, also the diurnal variation of the median and
standard deviation of the fit errors of all the data sets is shown in Fig. 2d. As demonstrated for other trace gas species in
345 Kreher et al. (2019), the DOAS fit errors and standard deviations of HONO delta SCDs should be comparable under ideal
conditions, which means different instruments measuring with exactly the same field of view (FOV) and acquisition time
under stable atmospheric conditions. However those ideal conditions can not be perfectly reached in reality. By comparing
350 Fig. 2c and Fig. 2d, one can see that the fit errors are smaller than the standard deviation of the HONO delta SCDs by ~ 0.3
 $\times 10^{15}$ molecules cm^{-2} , i.e. by about 50%. This feature indicates that the effects of atmospheric variability in the FOV of $\sim 1^\circ$
(corresponding to a round sky area with a radius of ~ 100 m under a frequent maximum visible distance of ~ 10 km) and
discrepancies of FOV and acquisition time between the different instruments can considerably contribute to random
discrepancies of HONO delta SCD measurements. A similar conclusion was obtained in the previous studies of Kreher et al.
355 (2019) and Bösch et al. (2018). The differences of random discrepancies and DOAS fit errors depend on actual instrumental
noise levels, measured species, and atmospheric variability conditions. Regarding the dependence on measured species,
Kreher et al. (2019) reported that random discrepancies of NO_2 dSCDs in the visible range is larger than DOAS fit errors by
an order of magnitude. Comparisons of DOAS fit errors and random discrepancies of HONO delta SCDs will be discussed
for individual instruments in section 3.3.1.

360 In order to evaluate the effect of clouds on the consistency of the HONO delta SCDs between the different data sets, we
show the diurnal variation of the median values of the HONO delta SCDs, corresponding standard deviations, and the
median and standard deviations of the DOAS fit errors separately calculated for measurements under “clear sky” and
“cloudy sky” conditions (see Sect. 2.4 about the cloud classification) in Fig. 2. In general, similar values of all the quantities
are found for both sky conditions, probably due to that HONO abundances are mostly near ground level and HONO
365 absorption light paths are not considerably affected by clouds located at high altitudes. However, for the standard deviation
of the HONO delta SCDs, larger values are found under “cloudy sky” conditions than under “clear sky” conditions. The
standard deviation of the DOAS fit error under “cloudy sky” conditions is larger than under “clear sky” conditions. This
finding might be attributed to two factors: 1) the rapid variation of cloud properties for conditions of inhomogeneous cloud
coverage; 2) the enhanced photon shot noise, due to the fact that less photons are received by instruments under “cloudy
370 sky” conditions, can result in larger random noise and further larger discrepancies of HONO delta SCDs between different
instruments compared to those under “clear sky” conditions. In addition, results similar to that shown in Fig. 2 are also
observed for the data sets retrieved using the “daily noon FRS”. Hence, we only show the results of using the “sequential
FRS”.

3.3 Comparison results for individual participants

375 For the data sets of HONO delta SCDs from individual participants, linear regressions against the median values are
calculated for the whole campaign. The corresponding correlation coefficients, slopes, intercepts, and the root mean square
(RMS) of the residuals are shown in Fig. 3a, b, c, and d, respectively. The corresponding median values and standard
deviations are presented in Fig. 3e. The median values and standard deviations of the DOAS fit error are shown in Fig. 3f.
For the intercepts, RMS, median differences, and fit errors shown in Fig. 3d, e, and f, a second y-scale is added on the right
380 side of the diagrams. It indicates the typical relative discrepancy compared to a typical high value of the HONO delta SCDs
of 2×10^{15} molecules cm^{-2} . This quantity is referred to as “typical percentage” in the subsequent part of this section. Since the



HONO profile retrievals are dominated by measurements at low elevation angles, the comparison results for 1° elevation are separately plotted in Fig. 3 (red and green dots). Also the comparison results for analyses using a “sequential FRS” or “daily noon FRS” are individually presented.

385 The discrepancies of the HONO delta SCDs between the different MAX-DOAS instruments consist of random and systematic discrepancies. The random discrepancies can be minimised by averaging over a large amount of measurements since instrumental noise and spatial-temporal variations of sky conditions and pollutants can be smoothed out by the averaging. The effect has been studied in Peters et al. (2019). In Fig. 3d, the RMS values of residuals of linear regressions against the median values can represent the random measurement errors similar as the standard deviations of HONO delta
390 SCDs discussed in section 3.2, whereas the slopes, intercepts, and median differences shown in Fig. 3b, c, and e indicate the systematic discrepancies. For comparisons with the RMS values, the DOAS fit errors from individual participants are also shown in Fig. 3f.

3.3.1 Random discrepancies

The RMS values shown in Fig. 3d for HONO delta SCDs are lower than $\sim 0.6 \times 10^{15}$ molecules cm^{-2} for most of the
395 participants, corresponding to a “typical percentage” of 30%. The RMS obtained using a “sequential” FRS and a “daily noon FRS” are similar in magnitude for most of the participants if all elevation angles or only the 1° elevation angle are considered. The lowest RMS values of $\sim 0.3 \times 10^{15}$ molecules cm^{-2} , corresponding to a “typical percentage” of 15%, are reached by the “BIRA”, “NIWA (2)”, “AMOIAP”, and, “NIWA (1)” instruments. Even though, the “NIWA (1)” instrument belongs to the group of “EnviMes” instruments, a lower RMS is reached by the “NIWA (1)” instrument compared to the
400 other “EnviMes” instruments. The improved performance might be attributed to the customized productions and personalised operation of the individual “EnviMes” instruments, as well as different implementations of the DOAS fits by the individual participants. Another interesting finding for the “EnviMes” instruments is that, although the same set of spectra measured by the “USTC” instruments (see Table 1) are analysed by the “DLR” and “USTC” researchers, much larger RMS values and fit errors are found for the “DLR(1)” and “DLR(2)” results (especially for the “DLR(2)” results with
405 the “sequential FRS”) than for the “USTC(1)” and “USTC(2)”. This finding implies that random discrepancies between the data sets can be considerably attributed to the specific implementation of the DOAS fits by the individual participants. The previous study of Peters et al., 2017 demonstrated that differences in DOAS retrieval codes can result in discrepancies of retrieved NO_2 dSCDs and RMS residuals by up to 8% and 100%, respectively. Since optical depths of HONO absorptions are typically much lower than NO_2 , the effect of differences in DOAS retrieval codes and DOAS implementations by
410 individual participants on retrieved HONO dSCDs might be relatively larger than that on NO_2 . The “CMA” RMS values derived for a mini MAX-DOAS instrument are the largest (~ 1 to 1.7×10^{15} molecules cm^{-2}) corresponding to a “typical percentage” of 30% to 85%. The large RMS of “CMA” is consistent with its large fit error of $\sim 1 \times 10^{15}$ molecules cm^{-2} . Therefore, we conclude that the mini MAX-DOAS instruments can hardly reach the signal to noise requirements for HONO measurements.

415 Fig. 3g shows the ratios of DOAS fit errors and the RMS values for individual data sets. This relates to the discussion at the end of Sect. 3.2 on the differences of DOAS fit errors and random discrepancies, Fig. 3g indicates that the ratios are different for different data sets and in the range of 0.3 to 1.6. For most of the data sets, the ratios are lower than unity, indicating effects of atmospheric variability and discrepancies of instrumental FOV and acquisition time more dominate random discrepancies than the effect of instrumental noise given by DOAS fit errors. The lowest ratio of 0.3 is found for the “BIRA”
420 data set. It indicates that the dominant factors of the random discrepancies of the “BIRA” data set are atmospheric variability and instrumental discrepancies, but not instrumental noise.



3.3.2 Systematic discrepancies

For an overview of the systematic biases, median differences of the individual data sets of HONO delta SCDs from the median values are calculated and shown in Fig. 3e. These biases are mostly in the range of $\pm 0.3 \times 10^{15}$ molecules cm^{-2} , corresponding to a “typical percentage” of about $\pm 15\%$. The slopes derived from the linear regression mostly deviate from unity by about $\pm 20\%$ and the intercepts are mostly in the range of $\pm 0.3 \times 10^{15}$ molecules cm^{-2} , which corresponds to a “typical percentage” of about $\pm 15\%$. For the individual data sets, the median differences are generally consistent with the intercepts, but not the slopes. This finding is related to the fact that low and high HONO delta SCDs dominate the intercept and slope derived from the linear regression. Since low values are more frequent than large values, the median values of the differences are dominated by the lower HONO delta SCDs. Hence the intercepts and slopes mainly represent the systematic discrepancies of low and high values of the HONO delta SCDs, respectively, whereas the median differences indicate the general bias. For the datasets from “BIRA”, “MPIC”, “AIOFM”, “NIWA (2)”, “AMOIAIP”, “USTC (1)”, “USTC (2)”, and “LMU”, the median differences, slopes, and intercepts are all in the range of $\pm 0.3 \times 10^{15}$ molecules cm^{-2} , $\pm 20\%$ deviation from unity, and $\pm 0.3 \times 10^{15}$ molecules cm^{-2} , respectively, representing the corresponding typical ranges. Much larger biases of the slopes (~ 0.5) are found for the “BSU” data with “sequential FRS” than that for those with “daily noon FRS”. The reason for this finding is not yet identified. For the “DLR (1)” and “DLR (2)” data, although the median differences fall within the range of typical values, different biases (about plus 30% or minus 30% for large HONO delta SCDs, as indicated by the slopes) are found for “DLR (1)” with “daily noon FRS”, and the “DLR (2)” with the “sequential FRS” at 1° elevation angle, respectively. Considering that the “DLR” data are derived from the same set of spectra as the “USTC” data, the different implementations of the DOAS fits by both participants might have caused the different results. For the “CMA” data sets, although the deviations of the slopes from unity are within about 20%, the median differences and intercepts of about -0.5×10^{15} molecules cm^{-2} indicate a larger underestimation of low HONO delta SCDs than for the other participants. However, here it should be noted that the correlation coefficient is also rather low ($r \sim 0.6$).

In order to further characterize the diurnal variation of the discrepancies for the individual participants, the median and 25% and 75% percentiles of the differences of the HONO delta SCDs from the medians for elevation angles of 1° , 5° , and 15° , respectively, are shown in Fig. 4. The comparison results for the data sets with “sequential FRS” and “daily noon FRS” are shown in the subpanels (a) and (b). Considerable diurnal variations of the discrepancies are found for the “DLR”, “BSU”, and “CMA” data. For “DLR” data, negative and positive biases occur in the early morning and around noon, respectively, especially if a “sequential FRS” is used. Larger negative biases in the morning and in the afternoon are observed for “CMA”. Larger negative biases of the “BSU” data with “sequential FRS” appear in the morning, whereas the “BSU” data with “daily noon FRS” show larger negative biases around noon. Additionally, different biases for different elevation angles are found for some data. For instance, the discrepancies of the “AIOFM”, “NIWA (2)” and “USTC (2)” data are larger for the 1° elevation angle than for other elevation angles in the early morning.

In order to evaluate the effects of the FRS selection on the HONO delta SCDs, the median and percentiles of the differences of the HONO delta SCDs of both procedures are shown in Fig. 4c. The statistics of the differences are provided for different hours of the day and elevation angles of 1° , 5° , and 15° , respectively. For most of the data sets, including “BIRA”, “MPIC”, “Boulder”, “AIOFM”, “NIWA (2)”, “NIWA (1)”, “USTC (1)”, “USTC (2)”, the median values of the differences are usually in the range of $\pm 0.1 \times 10^{15}$ molecules cm^{-2} (corresponding to a “typical percentage” of 5%), while 25% and 75% percentiles are in the range of 0.2×10^{15} molecules cm^{-2} (corresponding to a “typical percentage” of 10%). For the “BSU” data, a large positive bias of $\sim 3 \times 10^{15}$ molecules cm^{-2} is found in the early morning and decreases afterwards. The reason for this finding is not yet identified. The median differences for both “DLR” data sets are in the range of $\pm 1.6 \times 10^{15}$ molecules cm^{-2} (corresponding to a “typical percentage” of $\sim \pm 80\%$), depending on time of a day, whereas the difference of 25% and 75% percentiles are about 1×10^{15} molecules cm^{-2} . However, considering the fact that both “DLR” and “USTC” data sets are derived from the same spectra, we conclude that the different effects of the FRS selection arise from the specific



465 implementations of DOAS fits. For the “CMA” data, the median differences are in the range of 0.2 to -0.4×10^{15} molecules cm^{-2} . This finding probably reflects the effects of instrumental instability.

In general, systematic discrepancies between the data sets are in the range of $\pm 0.3 \times 10^{15}$ molecules cm^{-2} , which is about half of the general random discrepancy of $\sim \pm 0.6 \times 10^{15}$ molecules cm^{-2} . For a typical high HONO delta SCD of 2×10^{15} molecules cm^{-2} , the typical relative systematic and random discrepancies are about 15% and 30%, respectively. The lowest
470 random discrepancy of $\sim 0.3 \times 10^{15}$ molecules cm^{-2} , which is comparable to the general systematic bias, can be reached by some instruments. For some data sets, the systematic differences are higher (up to $\pm 0.5 \times 10^{15}$ molecules cm^{-2}) probably due to an inappropriate implementation of the DOAS fit. For most instruments, the FRS selection is not critical, as the systematic differences between the HONO delta SCDs retrieved using the “sequential FRS” or “daily noon FRS” are typically in the range of $\pm 0.1 \times 10^{15}$ molecules cm^{-2} .

475

3.3.3 Discussion on effects of misalignments of elevation angles

Misalignments of elevation angles for individual instruments might result in discrepancies of HONO delta SCDs between the instruments. Since elevation misalignments might consist in systematic offsets and temporal changes for individual instruments, the resulting discrepancies of HONO delta SCDs might be both systematic and random. We estimated the
480 typical bias of HONO delta SCDs according to a typical misalignment of elevation angles during the CINDI-2 campaign. Donner et al (2019) characterized biases of elevation angles being mostly smaller than 0.4° for most of the MAX-DOAS instruments during the CINDI-2 campaign, based on scanning horizon and active light calibration methods applied to individual instruments. Figure 2b indicates that the largest change of HONO delta SCDs per elevation angle degree appears at the lowest elevation angles of 1° to 3° . Therefore effects of misalignments of elevation angles on measured HONO delta
485 SCDs are stronger at smaller elevation angles than at larger ones. Based on the typical dependence of HONO delta SCDs on elevation angles, the bias of HONO delta SCDs at 1° due to a typical elevation angle bias of 0.4° can be roughly estimated as $\sim 0.2 \times 10^{15}$ molecules cm^{-2} in the morning and $\sim 0.04 \times 10^{15}$ molecules cm^{-2} around noon, which are only a third of typical DOAS fit errors shown in Fig. 2d and 10% of typical random discrepancies shown in Fig. 2b. Furthermore, we do not observe correlation between the bias of HONO delta SCD from the median values and identified misalignments of elevation
490 angles for some instruments for which considerable elevation misalignments occurred during the campaign. Overall, the misalignments of elevation angles result in negligible discrepancies of HONO delta SCDs between the instruments.

4. Inter-comparison of tropospheric HONO vertical profiles

In this section we present the inter-comparison of vertical profiles of the HONO VMRs retrieved by the different participants with different inversion algorithms for the baseline retrieval settings (see section 2.3.1). An overview of the retrieved profiles
495 is presented in section 4.1. The overall statistics and comparison results for the individual participants are given in sections 4.2 and 4.3, respectively.

4.1 Overview of retrieved HONO profiles

Time series of the HONO profiles retrieved by the different participants between 6 to 17 UTC on individual days during the whole campaign are plotted in Fig. 5. This also includes all the profile results for the four comparison tasks described in
500 section 2.3.2. Although the HONO profiles were retrieved in the altitude range below 4 km, only the results below 1km are shown, because above 1km only very small HONO mixing ratios are retrieved. However, for the calculation and inter-comparison of the HONO VCDs (sections 4.2 and 4.3), the HONO profiles are integrated for the altitude range from 0 to 4 km. For the individual comparison tasks, the median values of the HONO profiles are calculated and also plotted in Fig. 5.



All data sets indicate that HONO usually accumulates near the surface. However, considerable discrepancies of the absolute values and diurnal variations can also be seen. The sky conditions identified from the MPIC MAX-DOAS measurements (see section 2.4) are shown in the bottom panel of Fig. 5. The gaps of results in Fig. 5 are due to the unavailability of data as the corresponding MAX-DOAS instruments were not operational or the profile inversion failed. For Task T2b, the “MPIC (MAPA valid)” data show much more gaps than the “MPIC (MAPA)” data since the quality flag criteria (Beirle et al., 2019) were applied to the “MPIC (MAPA valid)” data. For Task T1a and T1b, two versions of “BIRA” profile results are displayed and marked as “BIRA (v1)” and “BIRA (v2)”, and discussed in section 5.3. Since the “BIRA (v2)” data set is retrieved with more realistic measurement uncertainties than “BIRA (v1)”, it has been decided to only use the “BIRA (v2)” data set in the further inter-comparison analysis in sections 4.2 and 4.3.

4.2 Statistical inter-comparisons of HONO profiles, VCD and near-surface VMRs

4.2.1 Comparisons with median values

The diurnal variations of the median values of the HONO VCDs and near-surface VMRs for all the data sets are calculated for the individual tasks and plotted in Fig. 6a and b, respectively. A steep decrease of the HONO VCDs and near-surface VMRs from ~ 3 to $\sim 1.5 \times 10^{15}$ molecules cm^{-2} and from ~ 0.4 to ~ 0.1 ppb between 6 and 8 UTC is found, respectively. Afterwards, the VCDs and VMRs close to the surface stay at low values with a slight decrease until 16 UTC. Considering the significant decrease of HONO in the early morning, the median values of the HONO profiles before and after 7 UTC are separately shown in Fig. 6d, and e, respectively. Both figures indicate that the HONO VMRs above 0.6 km are close to zero. In addition, Fig. 6a and b indicate considerable differences of the median values of the different tasks, especially in the early morning before 8 UTC. These differences can primarily be attributed to differences of the input HONO delta SCDs and aerosol profiles used in the profile retrievals.

The 25% and 75% percentiles of the differences of the HONO VCDs, near-surface VMRs, and vertical profiles before and after 7 UTC compared to the median values are shown in Fig. 6a, b, d, and e, respectively, with different columns indicating the four tasks. The deviations between the different data sets are much smaller if the common HONO delta SCDs (task T2a and T2b) are used than if the HONO delta SCDs measured by individual instruments (task T1a and T1b) were used. For task T2a, the half interquartile range is mostly $\sim 5 \times 10^{13}$ molecules cm^{-2} (corresponding to $\sim 15\%$ to $\sim 30\%$ of the median values) for the VCDs, and ~ 0.02 ppb for the near-surface VMRs ($\sim 5\%$ to $\sim 20\%$ of the median values). For task T1a, the half interquartile range increased by about three times compared to those for task T2a. Therefore, we conclude that the discrepancies of the HONO delta SCDs can contribute to $\sim 30\%$ to 60% deviations of the HONO VCDs, and $\sim 10\%$ to 40% deviations of the near-surface VMRs results. The deviations are smaller than the typical relative deviations of HONO delta SCDs of 40-100% at low elevation angles, which arise due to the smoothing effect of the profile inversion. For both tasks T2a and T2b, the absolute deviations are larger in the morning than in the afternoon, but the relative deviations are similar due to larger HONO values in the morning. Also slightly larger interquartile ranges are found for task T2b than for task T2a, especially in the morning by $\sim 3 \times 10^{13}$ molecules cm^{-2} and ~ 0.04 ppb respectively. This indicates that the discrepancies of the aerosol retrievals can cause discrepancies of the HONO VCDs and near-surface VMRs by $\sim 50\%$. Similar ranges of percentiles are found for task T1a and T1b, indicating that the effects of using either a “sequential FRS” or “daily noon FRS” on the consistency of the HONO profile retrievals are not critical. The comparison results of HONO profiles shown in Fig. 6d and e indicate that deviations of the HONO VMRs between different data sets are negligible at altitudes above 0.4 km, where the HONO VMRs are also almost zero.



4.2.2 Comparisons with LP-DOAS

The statistical differences (the median values and 25% and 75% percentiles) of the near-surface HONO VMRs of the different data sets compared to the co-located LP-DOAS are shown in Fig. 6c. The LP-DOAS measurements and data for the comparisons are described in section 2.3.3. The median differences and half interquartile ranges are mostly in the range of ± 0.05 ppb ($\sim 10\%$ to $\sim 50\%$) and 0.1 ppb ($\sim 20\%$ to $\sim 100\%$) for the four tasks. Systematically larger interquartile ranges are found in the early morning.

4.2.3 Cloud effects on the HONO profile results

In order to evaluate effects of clouds on the consistency of the HONO profile retrieval results, all quantities in Fig. 6 are separately shown for the measurements under “clear sky” and “cloudy sky” conditions. In general, similar values for the upper and lower quartiles are found for both clear and cloudy sky conditions, except for task T1a and T1b. The interquartile ranges under “cloudy sky” conditions are $\sim 10\%$ larger than those under “clear sky” condition for task T1a and T1b, which is probably related to the larger random discrepancies of the HONO delta SCDs measured by different instruments (see Fig. 2c and section 3.2).

4.3 Comparison results for individual participants

For the HONO near-surface VMRs and VCDs derived from the profile retrievals of the individual participants, linear regressions against the median values are performed. The derived correlation coefficients, slopes, and intercepts, as well as the RMS of the residuals are shown in Fig. 7a and c. The median values and standard deviations of the differences of the individual data sets from the median values are also presented in Fig. 7a and c, and for the vertical profiles in the three altitude intervals of 0 km to 0.2 km, 0.2 km to 0.4 km, 0.4 km to 0.6 km in Fig. 8. For the intercepts, RMS, and median differences shown in Fig. 7, the corresponding “typical percentages” (relative differences compared to a typical large HONO near-surface VMR of 0.4 ppb and VCD of 3×10^{15} molecules cm^{-2}) are also shown (see y axis on the right side). Additionally, for the comparison results of the near-surface HONO VMRs versus the LP-DOAS measurements, the same parameters as shown in Fig. 7a and c are given in Fig. 7b. The same parameters as shown in Fig. 7a and c are derived from the comparisons of the modelled and measured HONO delta SCDs and shown in Fig. 7d. Following the discussion from in section 3.3, the random and systematic discrepancies of the profile retrieval results are discussed in the following.

4.3.1 Random discrepancies

The RMS of the differences shown in Fig. 7a and c indicate systematically smaller random discrepancies for tasks T2a and T2b than for tasks T1a and T1b. The RMS values of near-surface HONO VMRs are around 0.08 ppb ($\sim 20\%$) for all the data sets in task T1a and T1b. The RMS values of HONO VCDs are around 0.6×10^{15} molecules cm^{-2} ($\sim 20\%$) for most of data sets, with a maximum value of $\sim 0.9 \times 10^{15}$ molecules ($\sim 30\%$) found for USTC (1). In tasks T2a and T2b, the RMS for the near-surface HONO VMRs and VCDs is typically around 0.02 ppb ($\sim 5\%$) and 0.2×10^{15} molecules cm^{-2} ($\sim 7\%$), respectively. The largest RMS of the near-surface HONO VMRs and VCDs are 0.06 ppb ($\sim 15\%$) and 0.7×10^{15} molecules ($\sim 25\%$), respectively, which are found for “MPIC (PriAM)” and “MPIC (MAPA)”. However, the RMS decreases dramatically if quality flags are applied to the “MPIC (MAPA)” data to derive the “MPIC (MAPA valid)” data. The standard deviations of the differences of the vertical profiles against the median values shown in Fig. 8 indicate that the random discrepancies at altitudes above 0.2 km are mostly much smaller than close to the surface. The standard deviation is mostly around 0.02 ppb in the altitude grid of 0.2 to 0.4 km and almost zero at altitudes above 0.4 km. A relatively large deviation of ~ 0.15 ppb for “AIOFM” appears at high altitudes in tasks T1a. And significantly larger deviations at high altitudes are found for the “MPIC (MAPA)” data than the other data in task T2b. However, the quality controlled “MPIC (MAPA valid)” data show the similar deviations with the other data.



4.3.2 Systematic discrepancies

Fig. 7a and c show the median differences, intercepts, and slopes derived from the comparison of the HONO near-surface VMRs and VCDs. Similar to the HONO delta SCDs discussed in section 3.3.2, the overall systematic discrepancies of near-surface VMRs and VCDs for low and high values are indicated by the slopes and intercepts, respectively. The median differences indicate that the systematic discrepancies are mostly in the range of 20% for both tasks T1a and T1b, and 5% for both tasks T2a and T2b. The discrepancies of the VCDs are larger between the different data sets compared to the discrepancies of the near-surface VMRs, and the correlation coefficients of the comparisons of the VCDs are smaller than those of the comparisons of the near-surface VMRs. The near-surface VMRs are thus more consistent within the data sets than the VCDs. In addition, the discrepancies for the tasks T1a and T1b are 4 times larger than for the tasks T2a and T2b, which indicates that the discrepancies of the profile retrievals are dominated by the errors from the input HONO delta SCDs, and not by the profile inversion algorithms. Additionally, the similar level of discrepancies between tasks T1a and T1b, and tasks T2a and T2b indicate that the effects of the “FRS” selection and different aerosol retrievals on the discrepancies of the HONO profile retrievals are almost negligible.

The data sets with substantial systematic discrepancies will be discussed individually in the following. The “CMA” data sets show a systematic overestimation of up to ~45% compared to the median values. However, Fig. 3e indicates a systematic underestimation of the “CMA” delta SCDs compared with the median values. Since Fig. 7d indicates a significant systematic overestimation of the modelled HONO delta SCDs compared to the measured ones, we conclude that the implementation of the profile inversions is the dominant factor causing a substantial overestimation of the “CMA” profile results compared to the other data. For the “LMU” data set, an overall underestimation of the VCDs, even though the near-surface VMRs are well consistent, is found because the VMRs are systematically lower than the median values at high altitudes, which can be seen in Fig. 8.

The systematic and random discrepancies between the different HONO profile results are quite comparable, and typically in the range of 20% for tasks T1a and T1b and 5% for tasks T2a and T2b, with extreme discrepancies of ~40% for task T1a and T1b, and ~20% for task T2a and T2b.

4.3.3 Comparison with LP-DOAS

The comparison results of the near-surface HONO VMRs of the individual participants against those measured by the co-located LP-DOAS instrument are displayed in Fig. 7b. There the correlation coefficients, slopes, intercepts, and RMS of residuals derived from the linear regressions as well as the median differences against the LP-DOAS results are shown. The median differences and intercepts are consistent with those derived from the comparisons of the individual data sets against the median values (Fig. 7a). However, the slopes of the individual participants for tasks T1a and T1b are smaller than those derived from the comparisons against the median values (Fig. 7a). Therefore, in general all data sets systematically underestimate high near-surface HONO VMRs compared to the LP-DOAS results. Since the vertical layer measured by the LP-DOAS is consistent with the lowest vertical layer of the MAX-DOAS profile retrieval, the systematic differences might be mainly attributed to different air mass measured by the two techniques. It needs to be noted that MAX-DOAS typically measures the averaged HONO values in an effective light path of about 10km, whereas LP-DOAS measures the averaged HONO values in a light path of about 4 km between its telescope and reflector. Since the typical life time of HONO is only of the order of 20 min under daytime condition, strong HONO concentration horizontal inhomogeneities can be expected.

For the random differences of the individual data sets against the LP-DOAS measurements, in general similar RMS values are observed as those derived from the comparison against the median values (Fig. 7a) for tasks T1a and T1b. However, for tasks T2a and T2b, the RMS values for “BIRA”, “BIRA MMF”, and “AUTH” are much larger for the comparison with LP-DOAS than those for the comparison with the median values. Therefore, we conclude that the random discrepancies might be dominated by variations of HONO concentrations in the air mass measured by the LP-DOAS. Frequent variations of



625 HONO concentrations can be expected due to the short life time of HONO. The variations of HONO concentrations in the
air mass measured by the MAX-DOAS instrument can be smoothed due to averaging effect in a typical effective light path
of ~10km length.

5 Sensitivity studies of profile inversion

630 5.1 Sensitivity study on the effects of a priori profiles and the a priori covariance based on synthetic HONO delta SCDs

In this section we evaluate the influence of the a priori profile on the retrieval results based on synthetic HONO delta SCDs
simulated by the RTM SCIATRAN. For these simulations, three different HONO profiles are used. These profiles as well as
the other input parameters used for the RTM simulations are provided in section 2.3.4. Among the three participants of this
sensitivity study, “INTA” and “AUTH” used the “BePro” profile inversion algorithm whereas “MPIC” used the “PriAM”
635 profile inversion algorithm. While “BePro” uses a linear optimal estimation method, in “PriAM” a nonlinear optimal
estimation approach in logarithmic space is applied. We also evaluate the effect of different definitions of a priori covariance
(S_a). In the baseline setting, S_a is set to 100% of the a priori values for the diagonal terms. In the following this baseline
configuration of S_a is referred to as “a priori determined S_a ”. For the “BePro” algorithm, S_a is alternatively also set to a
constant value at all altitudes, which is 100% of the a priori value in the lowest altitude grid. This setting of S_a is referred to
640 as the “constant S_a ”. The alternative choice of S_a can theoretically decrease the constraints of the a priori profile on the
retrieved profiles. Here it should be noted that for “PriAM” the definition of S_a according to the baseline settings is changed
to unity at all altitudes due to its conversion to the logarithmic space. We don’t apply an alternative S_a for “PriAM”.

HONO profiles are retrieved from synthetic HONO delta SCDs using three different a priori profiles (shown in Fig. 1b) and
two different S_a . The retrieved profiles are shown in Fig. 9 separately for the three different algorithms. It is found that for
645 all scenarios similar results are retrieved by “INTA” and “AUTH”, which apply the same “BePro” algorithm. For the tests
with the a priori determined S_a , both “INTA” and “AUTH” considerably overestimate the HONO VMRs near the surface
and underestimate those at high altitudes for the profiles 2 and 3 if the a priori profile 3 is used. However, for the tests with
constant S_a , well consistent profile results are derived by “INTA” and “AUTH” for all three a priori profiles. This indicates
that the HONO profile retrievals using “BePro” respond to the true HONO profiles much better if a “constant S_a ” is used.
650 For the “MPIC” results with the “PriAM” algorithm, also well consistent profiles are obtained for the three different a priori
profiles. For profile 1 the “MPIC” retrieval agrees much better with the true profile than “INTA” and “AUTH” results. These
results indicate that the “PriAM” algorithm can better respond to different HONO profile shapes through the implementation
of the non-linear iterative procedure in logarithmic space.

The effect of random noise on the profile retrievals were tested based on the “noisy synthetic HONO delta SCDs”, which are
655 described in section 2.3.4. Median values and standard deviations of differences of the retrieved HONO profiles compared to
those retrieved from the synthetic HONO delta SCDs without noise are shown in Fig. 10. And for the same results, the ratios
of the median values and standard deviations shown in Fig. 10 compared to the true HONO profiles are plotted in Fig. 11.
The results for the retrievals using the “a priori determined S_a ” and “constant S_a ” are shown separately in Fig. 10 and Fig. 11.
For “INTA” and “AUTH”, much larger standard deviations for retrievals using the “constant S_a ” than those using the “a
660 priori determined S_a ” at high altitudes are found due to the smaller a priori constraints if the “constant S_a ” is used. For
“MPIC”, standard deviations at altitudes below 1 km are similar with those for “INTA” and “AUTH” with the “constant S_a ”.
However, much smaller standard deviations are found at altitudes above 1 km.

We conclude that for the “BePro” algorithm, the “constant S_a ” can increase the response of the profile retrievals to different
HONO profile shapes, but can reduce the stability. The “PriAM” algorithm can well balance the response and stability.
665 Therefore we recommend retrieving HONO profiles in logarithmic space.



5.2 Sensitivity study on the effects of the grid intervals in the profile retrievals

In the baseline settings of the profile retrievals the grid interval were set to 200 m. Since a significant vertical gradient might appear in the lowest 200 m, we tested the effects of using different grid intervals, e.g. 50m and 100m on the retrieved profiles using the “PriAM” algorithm based on the “MPIC” measured HONO delta SCDs during the whole campaign. For different grid intervals, the averaged diurnal variations of the retrieved HONO VMRs below 200 m are shown in Fig. 12a. Differences of the retrieved HONO VMRs using grid intervals of 100m and 50m compared to the baseline setting are shown in Fig. 12b. Fig 12 indicates that the retrieved HONO VMRs below 100 m for both retrievals with grid intervals of 50m and 100m are similar to those grid intervals of 200m (baseline settings). The retrieved HONO VMRs significantly decrease in the grids above 100m. Based on this sensitivity test, it is concluded that a finer resolution than 200m can improve the profile results in the altitudes range below 200m.

5.3 Measurement uncertainties of HONO dSCDs and their effects on profile retrievals.

In order to calculate the diagonal elements of the covariance matrix of measurement uncertainties for profile retrievals using the optimal estimation method, measurement uncertainties of HONO dSCDs need to be estimated. Measurement uncertainties can be mainly attributed to instrumental noise and atmospheric variability. DOAS fit errors provide a good representation of the instrumental noise. In the baseline settings of profile retrievals, we assume that measurement uncertainties and DOAS fit errors of HONO dSCDs are equivalent. However this assumption is not realistic if the effect of atmospheric variability is significantly larger than DOAS fit errors. As shown in Fig. 3f, the lowest DOAS fit errors of $\sim 0.1 \times 10^{15}$ molecules cm^{-2} are found for the BIRA instrument, and they are three times lower than the typical DOAS fit error of $\sim 0.3 \times 10^{15}$ molecules cm^{-2} of the other instruments as shown in Fig. 2c. Two data sets of HONO profile results are derived from the same HONO dSCD data sets with different settings of the diagonal elements of the measurement uncertainty covariance matrix. The baseline profile retrieval settings (i.e. 100% of the DOAS fit errors of the HONO dSCDs) are applied for the retrievals of the “BIRA (v1)” data set., while the “BIRA (v2)” data sets corresponds to the bePRO profile retrievals where 300% of the DOAS fit errors of the HONO dSCDs are used. Fig. 5 indicates that the “BIRA (v1)” results deviate more from the median values than those of “BIRA (v2)”. This feature is due to the fact that the measurement uncertainties of the “BIRA” instrument are substantially larger than its DOAS fit errors, due to the effect of atmospheric variability. In order to realistically estimate measurement uncertainties, the standard deviations of the “BIRA” HONO dSCDs retrieved using the daily noon FRS in the time period of 11 to 16 UTC on individual days are shown in Fig. 13a. Since HONO dSCDs, especially in the zenith view, are close to zero as shown in Fig. 2b, the standard deviations can represent random measurement uncertainties. Since the DOAS fit errors of the “MPIC” data set are in the moderate range of all the participating instruments, the standard deviations of the “MPIC” data set are calculated and shown in Fig. 13b for comparisons with the “BIRA” data set. In addition, the averaged DOAS fit errors of HONO dSCDs of both data sets are shown in the bottom panel of Fig. 13. Figure 13 indicates that although the DOAS fit errors of the “BIRA” data set is about one third of the “MPIC” data set, the standard deviations of both the “MPIC” and “BIRA” data set are comparable and around 0.2 to 0.3×10^{15} molecules cm^{-2} . This feature suggests that measurements uncertainties are similar for both the “MPIC” and “BIRA” data sets due to the dominant effect of atmospheric variability on the measurement uncertainties of the “BIRA” data sets. In contrast to the “BIRA” case, both atmospheric variability and instrumental noise are comparable in the “MPIC” data set. Since the measurement uncertainties are about three times higher than the DOAS fit errors for the “BIRA” instrument, the setting for the “BIRA (v2)” profile results is more realistic that for the “BIRA (v1)” profile results. However for the “MPIC” instrument and most of the other instruments, since the measurement uncertainties are comparable to the DOAS fit errors, baseline settings are reasonable. We can conclude that not only DOAS fit errors, but also atmospheric variability should be considered for the estimation of measurement uncertainties for profile retrievals. The effect of atmospheric variability on measurement uncertainties of HONO dSCDs is roughly around 0.2 to 0.3×10^{15} molecules cm^{-2} ,



which might be significantly larger than DOAS fit errors of a state-of-art MAX-DOAS instrument with high signal to noise ratios.

710

6 Conclusions

In this study, HONO delta SCDs and vertical profiles are retrieved from different MAX-DOAS observations during the CINDI-2 campaign. VCDs and near-surface VMRs are derived using different profile inversion algorithms, which are applied to HONO delta SCDs analysed by the different participants. Peak HONO values with delta SCDs at 1° elevation angle of $\sim 3 \times 10^{15}$ molecules, VCDs of 3×10^{15} molecules cm^{-2} , and near-surface VMRs of 0.4 ppb on average are retrieved in the early morning. These are followed by a steep decrease to $\sim 1.2 \times 10^{15}$ molecules cm^{-2} , $\sim 1.5 \times 10^{15}$ molecules cm^{-2} , ~ 0.1 ppb, respectively, during the period from 6 to 8 UTC. Afterwards, the HONO values stay low and further decrease slightly during the rest of the day. The profile results indicate that most of HONO accumulates at altitudes below 0.2 km and HONO concentrations are close to zero at altitudes above 0.4 km during the day.

715

720

We evaluated random and systematic differences between different retrieval results of HONO delta SCDs derived from different MAX-DOAS instruments using different inversion algorithms. For MAX-DOAS instruments with a good spectrometer, the systematic discrepancies of the delta SCDs of the different MAX-DOAS instruments are generally in the range of $\pm 0.3 \times 10^{15}$ molecules cm^{-2} , which is half of the typical random uncertainty of $\sim 0.6 \times 10^{15}$ molecules cm^{-2} . For a typical high value of HONO delta SCD of 2×10^{15} molecules cm^{-2} , the typical relative systematic and random uncertainties are about 15% and 30%, respectively. Similar magnitudes of random and systematic uncertainties are observed for different elevation angles. However, since the HONO delta SCDs decrease with increasing elevation angle the relative random and systematic uncertainties reach up to 200% - 400%, and 100% - 200%, respectively, for the 30° elevation angle. The HONO delta SCDs retrieved by some participants show substantially larger random and systematic discrepancies compared to most participants, which is mainly caused by limitations of the instrumental signal to noise ratios or an inappropriate implementation of DOAS fits. Another important finding is that for most instruments the random discrepancies of HONO delta SCD results between the different instruments are significantly larger than individual DOAS fit errors due to the effects of atmospheric variability and discrepancies of instrumental FOV and acquisition time. In addition, for most of the instruments, the effects of using either a “sequential FRS” or “daily noon FRS” on the errors of the HONO delta SCDs is practically negligible with systematic and random differences between both retrieval results typically within $\pm 0.1 \times 10^{15}$ molecules cm^{-2} ($\sim \pm 5\%$).

725

730

735

Random and systematic differences between the retrieved HONO VCDs, near-surface VMRs, and profiles from the different MAX-DOAS instruments and inversion algorithms are further evaluated via statistical inter-comparison. Both systematic and random differences of HONO VCDs and near-surface VMRs are typically $\sim 20\%$. For some instruments, the maximum random and systematic discrepancies are $\sim 40\%$. In order to better understand the reasons for the differences, all participants retrieved HONO profiles also from a set of common HONO delta SCDs using their specific inversion algorithms. The results of this task indicate that the differences of the profile inversion algorithms generally contribute to both systematic and random discrepancies of the HONO VCDs to about $\sim \pm 0.2 \times 10^{15}$ molecules cm^{-2} and of the near-surface VMRs to about $\sim \pm 0.02$ ppb (typically $\sim 5\%$ for both VCDs and near-surface VMRs). These results indicate that the errors of the HONO delta SCDs dominate the differences of HONO profile results. Further error sources, especially for the most extreme discrepancies, are probably inappropriate implementations of the profile inversion algorithms and/or configurations of the profile retrievals. Both systematic and random discrepancies are considerably higher in the lowest altitude range of 0 to 0.2 km, mostly ~ 0.02 ppb in the altitude range from 0.2 to 0.4 km and almost zero above. In addition, the effect of using a

740

745



“daily noon FRS” or a “sequential FRS” in the DOAS fit on the profile results is almost negligible. Also the effect of different aerosol retrievals on HONO profile results is typically negligible.

750 The near-surface HONO VMRs retrieved from different MAX-DOAS measurements are also compared to the co-located LP-DOAS measurements. In general, the systematic discrepancies of the individual MAX-DOAS measurements compared to the LP-DOAS results are similar to those derived from the comparison with the median values of all MAX-DOAS results. Interestingly, the median values of all MAX-DOAS measurements are systematically lower or higher than the LP-DOAS results by up to 0.15 ppb (~50%) and 0.07 ppb (~20% - 200%) in the early morning and around noon, respectively.

755 The effects of a priori profiles and covariance for the “BePro” and “PriAM” profile inversion algorithms, which are both based on the optimal estimation method but in linear and logarithmic space respectively, were evaluated using simulated delta SCDs for three different altitude profiles. The results of this sensitivity study indicate that a “constant Sa” for the “BePro” algorithm in linear space can increase the response of the profile retrievals to different HONO profile shapes, but tends to reduce the stability. The “PriAM” algorithm in logarithmic space can well balance the response and stability.

760 Therefore we recommend retrieving HONO profiles in logarithmic space. Additional sensitivity tests indicate that a finer resolution than 200m improve the retrieved profiles in the altitudes range below 200m. In addition it is found that measurement uncertainties of HONO dSCDs, which are needed to calculate measurement uncertainty covariance matrix for profile retrievals using the optimal estimation method, can be significantly larger than DOAS fit errors due to the effect of atmospheric variability, especially for an instrument with a low noise level. This may lead to unrealistic estimations of measurement uncertainties causing considerable discrepancies in profile results. Therefore, not only DOAS fit errors, but also the effect of atmospheric variability needs to be considered for the estimation of measurement uncertainties. The typical contribution of atmospheric variability to measurement uncertainties is about 2 to 3×10^{15} molecules cm^{-2} , but it might depend on particular sky conditions and instrumental properties.

765 We summarise that, even though the errors of the measured HONO delta SCDs usually dominate the errors of the retrieved HONO profiles, also the inappropriate implementation of the profile inversion algorithms can cause substantial discrepancies. Profile inversion algorithms with proper configuration can well retrieve different HONO profile shapes, especially in logarithmic space. This corroborates that one important feature of the retrieved HONO profiles, the high concentrations near the surface, represents well the ambient HONO vertical distribution during the CINDI-2 campaign.

770 Author contributions. Y. Wang prepared the paper with contributions from all co-authors. All co-authors contributed to modifications and discussions in preparing the manuscript. Individually S. Donner, T. Wagner, and Y. Wang operated the instrument and evaluated data of the MPIC group. Steffen Beirle performed the profile inversion with the MAPA algorithm. A. Hilboll performed the radiative transfer simulations for the synthetic dSCDs. Stefan Schmitt prepared and operated the LP-DOAS instrument and evaluated the corresponding data. C. Zhang, Z. Wang and K.L. Chan operated the USTC-DLR instruments. C. Zhang, Z. Wang, H. Liu, C. Xing and C. Liu evaluated the USTC-DLR measurement data. C. Liu managed all the USTC-DLR activities. K.L. Chan operated the LMU instrument and evaluated the measurement data. T. Drosoglou and A. Bais operated the instrument and evaluated data of the Aristotle University of Thessaloniki. P. Johnston and R. Querel each operated a MAXDOAS instrument and processed its data on behalf of the NIWA group. M. Van Roozendael and F. Hendrick contributed to the design and planning of the CINDI-2 campaign, operated a MAX-DOAS instrument, evaluated SCD and profile data on behalf of the BIRA group. M. M. Friedrich performed the profile retrievals using the MMF algorithm. N. Benavent, D. Garcia-Nieto and A. Saiz-Lopez operated the instrument and evaluated data from the Department of Atmospheric Chemistry and Climate, IQFR-CSIC. J. L. Jin and J. Z. Ma operated the instrument and evaluated data of the CMA. A. Borovski and O. Postlyakov operated AMOIAP instrument and evaluated its data. M. Yela provided financial support and resources and scientific discussion for the INTA group. L. Gómez-Martín performed vertical profiles simulations of INTA. J. L. Tirpitz contributed to the graphical representation of the inter-comparison results

775
780
785
790



and the scientific discussion. T. Koenig and H. Finkenzeller and R. Volkamer operated the instruments and evaluated data for CU Boulder. K. Kreher was the referee for the CINDI-2 inter-comparison campaign and as such involved in the day-to-day campaign management and data quality checks of all CINDI-2 MAX-DOAS measurements. J. Xu, X. Tian and P. Xie operated the instrument and evaluated data of Anhui Institute of Optics and Fine Mechanics (AIOFM).

795

Acknowledgements. We gratefully acknowledge the KNMI staff at Cabauw for their excellent technical and infrastructure support during the campaign. Funding for this study was provided by ESA through the CINDI-2 (ESA Contract No.4000118533/16/I-Sbo) and FRM4DOAS (ESA Contract No. 4000118181/16/I-EF) projects. We would like to thank Marc Allaart for the provision of pressure and temperature sonde measurements in De Bilt via the NDACC database. CMA group acknowledge the support by the NSFC under project Nos.41805027. Work of AMOIAP group was supported by the Russian Foundation for Basic Research (grant no. 18-35-00682) and the Russian Academy of Sciences (grant no. 0150-2018-0052). SCIATRAN simulations were performed on the HPC cluster Aether at the University of Bremen, financed by DFG in the scope of the Excellence Initiative. R. Volkamer acknowledges funding from NASA's Atmospheric Composition Program (NASA-16-NUP2016-0001), and US National Science Foundation (award AGS-1620530). H. Finkenzeller is recipient of a NASA graduate fellowship. Work of AMOIAP group was supported by the Russian Foundation for Basic Research (grant no. 18-35-00682) and the Russian Academy of Sciences (grant no. 0129-2019-0002). K.L. Chan has received funding from the European Union's Horizon 2020 research and innovation programme through the ACTRIS-2 transnational access programme (Grant No. 654109). The AIOFM group acknowledges the support by the NSFC (grant no. 41530644).

References

- Arnoud Apituley, Francois Hendrick, Michel van Roozendael, Andreas Richter, Thomas Wagner, Udo Friess, Karin Kreher, Mirjam den Hoed, Deborah Stein-Zweers, Henk Eskes, Rinus Scheele, Ankie Piters, Marc Allaart, Shreyans Jain, Anam Bloch, Arnoud Frumau, Aleis Merlaud, Frederic Tack, Johannes Lampel, Stefan Schmitt, Jan-Lucas Tirpitz, Jan Vonk, Stijn Berkhout, Rene van der Hoff, Daan Swart.: Second Cabauw Intercomparison of Nitrogen Dioxide Measuring Instruments (CINDI-2) -- Campaign Overview, *Atm. Meas. Tech.*, in preparation, 2019.
- Acker, K., Möller, D., Wieprecht, W., Meixner, F.X., Bohn, B., Gilge, S., Plass - Dülmer, C. and Berresheim, H.: Strong daytime production of OH from HNO₂ at a rural mountain site, *Geophysical Research Letters*, 33(2), doi: 10.1029/2005GL024643, 2006.
- Akimoto, H., Takagi, H., and Sakamaki, F.: Photoenhancement of the nitrous acid formation in the surface reaction of nitrogen dioxide and water vapor: Extra radical source in smog chamber experiments, *Int. J. Chem. Kinet.*, 19, 539-551, doi:10.1002/kin.550190606, 1987.
- Alicke, B., Geyer, A., Hofzumahaus, A., Holland, F., Konrad, S., Pätz, H.W., Schäfer, J., Stutz, J., Volz - Thomas, A. and Platt, U.: OH formation by HONO photolysis during the BERLIOZ experiment, *Journal of Geophysical Research: Atmospheres*, 108(D4), doi:10.1029/2001JD000579, 2003.
- Aliwell, S. R., Van Roozendael, M., Johnston, P. V., Richter, A., Wagner, T., Arlander, D. W., Burrows, J. P., Fish, D. J., Jones, R. L., Tørnkvist, K. K., Lambert, J.-C., Pfeilsticker, K., and Pundt, I.: Analysis for BrO in zenith-sky spectra: An inter-comparison exercise for analysis improvement, *J. Geophys. Res.*, 107, D140, doi:10.1029/2001JD000329, 2002.
- Bösch, T., Rozanov, V., Richter, A., Peters, E., Rozanov, A., Wittrock, F., Merlaud, A., Lampel, J., Schmitt, S., de Haij, M., Berkhout, S., Henzing, B., Apituley, A., den Hoed, M., Vonk, J., Tiefengraber, M., Müller, M., and Burrows, J. P.:



- BOREAS – a new MAX-DOAS profile retrieval algorithm for aerosols and trace gases, *Atmos. Meas. Tech.*, 11, 6833-6859, <https://doi.org/10.5194/amt-11-6833-2018>, 2018.
- 835 Beirle, S., Dörner, S., Donner, S., Remmers, J., Wang, Y., and Wagner, T.: The Mainz profile algorithm (MAPA), *Atmos. Meas. Tech.*, 12, 1785-1806, <https://doi.org/10.5194/amt-12-1785-2019>, 2019.
- Bobrowski, N., Hönninger, G., Galle, B. and Platt, U.: Detection of bromine monoxide in a volcanic plume, *Nature*, 423, 273-276, 2003.
- Bogumil, K., Orphal, J., Homann, T., Voigt, S., Spietz, P., Fleischmann, O. C., Vogel, A., Hartmann, M., Kromminga, H., Bovensmann, H., Frerick, J., and Burrows, J. P.: Measurements of molecular absorption spectra with the SCIAMACHY pre-flight model: instrument characterization and reference data for atmospheric remote-sensing in the 230–2380 nm region, *J. Photoch. Photobio. A*, 157, 167-184, 2003.
- 840 Burrows, J.P., Dehn, A., Deters, B., Himmelmann, S., Richter, A., Voigt, S. and Orphal, J.: Atmospheric remote-sensing reference data from GOME: Part 1. Temperature-dependent absorption cross-sections of NO₂ in the 231–794 nm range, *Journal of Quantitative Spectroscopy and Radiative Transfer*, 60(6), 1025-1031. 1998.
- 845 Chan, K. L., Wiegner, M., Wenig, M., and Pöhler, D.: Observations of tropospheric aerosols and NO₂ in Hong Kong over 5 years using ground based MAX-DOAS, *Science of The Total Environment*, 619-620, 1545 – 1556, <https://doi.org/https://doi.org/10.1016/j.scitotenv.2017.10.153>, 2018
- Clémer, K., Van Roozendaal, M., Fayt, C., Hendrick, F., Hermans, C., Pinardi, G., Sperr, R., Wang, P., and De Maziere, M.: Multiple wavelength retrieval of tropospheric aerosol optical properties from MAXDOAS measurements in Beijing, 850 *Atmos. Meas. Tech.*, 3, 863–878, 2010.
- Danckaert, T., Fayt, C., Van Roozendaal, M., De Smedt, I., Letocart, V., Merlaud, A., and Pinardi, G.: QDOAS Software User Manual Version 3.2, Belgian Institute for Space Aeronomy (BIRA-IASB), 2017.
- Donner, S. : Mobile MAX-DOAS measurements of the tropospheric formaldehyde column in the Rhein – Main Region, Master Thesis, Institute for Atmospheric Physics of the Johannes Gutenberg University Mainz, 2016.
- 855 Donner, S., Kuhn, J., Van Roozendaal, M., Bais, A., Beirle, S., Bösch, T., Bogner, K., Bruchkousky, I., Chan, K. L., Drosoglou, T., Fayt, C., Frieß, U., Hendrick, F., Hermans, C., Jin, J., Li, A., Ma, J., Peters, E., Pinardi, G., Richter, A., Schreier, S. F., Seyler, A., Strong, K., Tirpitz, J.-L., Wang, Y., Xie, P., Xu, J., Zhao, X., and Wagner, T.: Evaluating different methods for elevation calibration of MAX-DOAS instruments during the CINDI-2 campaign, *Atmos. Meas. Tech. Discuss.*, <https://doi.org/10.5194/amt-2019-115>, in review, 2019.
- 860 Emde, C., Buras-Schnell, R., Kylling, A., Mayer, B., Gasteiger, J., Hamann, U., Kylling, J., Richter, B., Pause, C., Dowling, T., and Bugliaro, L.: The libRadtran software package for radiative transfer calculations (version 2.0.1), *Geosci. Model Dev.*, 9, 1647-1672, <https://doi.org/10.5194/gmd-9-1647-2016>, 2016.
- Elshorbany, Y.F., Kleffmann, J., Kurtenbach, R., Lissi, E., Rubio, M., Villena, G., Gramsch, E., Rickard, A.R., Pilling, M.J. and Wiesen, P.: Seasonal dependence of the oxidation capacity of the city of Santiago de Chile, *Atmospheric Environment*, 44(40), 5383-5394, 2010.
- 865 Fayt, C. and van Roozendaal, M.: WinDOAS 2.1 Software User Manual, IASB/BIRA (<http://www.oma.be/GOME/GOMEBro/WinDOAS-SUM-210b.pdf>), 2009.
- Fleischmann, O. C., Hartmann, M., Burrows J. P., and Orphal, J.: New ultraviolet absorption cross-sections of BrO at atmospheric temperatures measured by time-windowing Fourier transform spectroscopy, *J. Photochem. Photobiol. A*, 870 168, 117–132, 2004.
- Friedrich, M. M., Rivera, C., Stremme, W., Ojeda, Z., Arellano, J., Bezanilla, A., García-Reynoso, J. A., and Grutter, M.: NO₂ vertical profiles and column densities from MAX-DOAS measurements in Mexico City, *Atmos. Meas. Tech.*, 12, 2545-2565, <https://doi.org/10.5194/amt-12-2545-2019>, 2019.



- Frieß, U., Monks, P. S., Remedios, J. J., Rozanov A., Sinreich R., Wagner T., and Platt, U.: MAX-DOAS O₄ measurements:
875 A new technique to derive information on atmospheric aerosols: 2. Modeling studies, *J. Geophys. Res.*, 111, D14203,
doi:10.1029/2005JD006618, 2006.
- Frieß U, Sihler H, Sander R. The vertical distribution of BrO and aerosols in the Arctic: Measurements by active and passive
differential optical absorption spectroscopy, *J. Geophys. Res.*, 116, D00R04, 2011.
- Frieß, U., Klein Baltink, H., Beirle, S., Clémer, K., Hendrick, F., Henzing, B., Irie, H., de Leeuw, G., Li, A., Moerman, M.
880 M., van Roozendaal, M., Shaiganfar, R., Wagner, T., Wang, Y., Xie, P., Yilmaz, S., and Zieger, P.: Inter-comparison of
aerosol extinction profiles retrieved from MAX-DOAS measurements, *Atmos. Meas. Tech.*, 9, 3205-3222,
https://doi.org/10.5194/amt-9-3205-2016, 2016.
- Frieß, U., Beirle, S., Alvarado Bonilla, L., Bösch, T., Friedrich, M. M., Hendrick, F., PETERS, A., Richter, A., van Roozendaal,
M., Rozanov, V. V., Spinei, E., Tirpitz, J.-L., Vlemmix, T., Wagner, T., and Wang, Y.: Intercomparison of MAX-DOAS
885 vertical profile retrieval algorithms: studies using synthetic data, *Atmos. Meas. Tech.*, 12, 2155-2181,
https://doi.org/10.5194/amt-12-2155-2019, 2019.
- Hartl, A. and Wenig, M. O.: Regularisation model study for the least-squares retrieval of aerosol extinction time series from
UV/VIS MAX-DOAS observations for a ground layer profile parameterisation, *Atmos. Meas. Tech.*, 6, 1959-1980,
doi:10.5194/amt-6-1959-2013, 2013.
- 890 Hendrick, F., Müller, J.-F., Clémer, K., Wang, P., De Mazière, M., Fayt, C., Gielen, C., Hermans, C., Ma, J. Z., Pinardi, G.,
Stavrakou, T., Vlemmix, T., and Van Roozendaal, M.: Four years of ground-based MAX-DOAS observations of
HONO and NO₂ in the Beijing area, *Atmos. Chem. Phys.*, 14, 765-781, doi:10.5194/acp-14-765-2014, 2014.
- Hönninger, G. and Platt, U.: Observations of BrO and its vertical distribution during surface ozone depletion at Alert, *Atmos.*
Environ., 36, 2481-2489, 2002.
- 895 Hönninger, G., Friedeburg, C. von and Plat, U., Multi axis differential optical absorption spectroscopy (MAX-DOAS),
Atmos. Chem. Phys., 4, 231-254, 2004.
- Irie, H., Kanaya, Y., Akimoto, H., Iwabuchi, H., Shimizu, A., and Aoki, K.: First retrieval of tropospheric aerosol profiles
using MAX-DOAS and comparison with lidar and sky radiometer measurements, *Atmos. Chem. Phys.*, 8, 341-350, 2008.
- Irie, H., Takashima, H., Kanaya, Y., Boersma, K. F., Gast, L., Wittrock, F., Brunner, D., Zhou, Y., and Van Roozendaal, M.:
900 Eight-component retrievals from ground-based MAX-DOAS observations, *Atmos. Meas. Tech.*, 4, 1027-1044, 2011.
- Jin, J., Ma, J., Lin, W., Zhao, H., Shaiganfar, R., Beirle, S. and Wagner, T.: MAX-DOAS measurements and satellite
validation of tropospheric NO₂ and SO₂ vertical column densities at a rural site of North China, *Atmospheric*
Environment, 133, 12-25, 2016a.
- Jin J., Ma, J., Lin, W., Zhao, H.: Characteristics of NO₂ Tropospheric column density over a rural area in the North China
905 Plain (in Chinese), *J. Appl. Meteor. Sci.*, 27(3), 303-311, doi:10.11898/1001-7313.20160305, 2016b.
- Kanaya, Y., Irie, H., Takashima, H., Iwabuchi, H., Akimoto, H., Sudo, K., Gu, M., Chong, J., Kim, Y. J., Lee, H., Li, A., Si,
F., Xu, J., Xie, P.-H., Liu, W.-Q., Dzhola, A., Postlyakov, O., Ivanov, V., Grechko, E., Terpigova, S., and Panchenko,
M.: Long-term MAX-DOAS network observations of NO₂ in Russia and Asia (MADRAS) during the period 2007-2012:
instrumentation, elucidation of climatology, and comparisons with OMI satellite observations and global model
910 simulations, *Atmos. Chem. Phys.*, 14, 7909-7927, doi:10.5194/acp-14-7909-2014, 2014.
- Kleffmann, J., Gavriloaiei, T., Hofzumahaus, A., Holland, F., Koppmann, R., Rupp, L., Schlosser, E., Siese, M. and Wahner,
A.: Daytime formation of nitrous acid: A major source of OH radicals in a forest, *Geophysical Research Letters*, 32(5),
doi: 10.1029/2005GL022524, 2005.
- Kraus, S.: DOASIS, A Framework Design for DOAS, PhD-thesis, University of Mannheim, [http://hci.iwr.uni-](http://hci.iwr.uni-heidelberg.de/publications/dip/2006/Kraus_PhD2006.pdf)
915 [heidelberg.de/publications/dip/2006/Kraus_PhD2006.pdf](http://hci.iwr.uni-heidelberg.de/publications/dip/2006/Kraus_PhD2006.pdf), 2006.



- 920 Kreher, K., Van Roozendael, M., Hendrick, F., Apituley, A., Dimitropoulou, E., Frieß, U., Richter, A., Wagner, T.,
Abuhassan, N., Ang, L., Anguas, M., Bais, A., Benavent, N., Bösch, T., Bognar, K., Borovski, A., Bruchkouski, I., Cede,
A., Chan, K. L., Donner, S., Drosoglou, T., Fayt, C., Finkenzeller, H., Garcia-Nieto, D., Gielen, C., Gómez-Martín, L.,
Hao, N., Herman, J. R., Hermans, C., Hoque, S., Irie, H., Jin, J., Johnston, P., Khayyam Butt, J., Khokhar, F., Koenig, T.
925 K., Kuhn, J., Kumar, V., Lampel, J., Liu, C., Ma, J., Merlaud, A., Mishra, A. K., Müller, M., Navarro-Comas, M.,
Ostendorf, M., Pazmino, A., Peters, E., Pinardi, G., Pinharanda, M., Piters, A., Platt, U., Postlyakov, O., Prados-Roman,
C., Puentedura, O., Querel, R., Saiz-Lopez, A., Schönhardt, A., Schreier, S. F., Seyler, A., Sinha, V., Spinei, E., Strong,
K., Tack, F., Tian, X., Tiefengraber, M., Tirpitz, J.-L., van Gent, J., Volkamer, R., Vrekoussis, M., Wang, S., Wang, Z.,
Wenig, M., Wittrock, F., Xie, P. H., Xu, J., Yela, M., Zhang, C., and Zhao, X.: Intercomparison of NO₂, O₄, O₃ and
HCHO slant column measurements by MAX-DOAS and zenith-sky UV-Visible spectrometers during the CINDI-2
campaign, *Atmos. Meas. Tech. Discuss.*, <https://doi.org/10.5194/amt-2019-157>, in review, 2019.
- Kurucz, R.L., Furenid, I., Brault, J. and Testerman, L.: *Solar Flux Atlas from 296 to 1300 nm*, in *National Solar
Observatory Atlas*, Harvard Univ., Cambridge, Mass, 1984.
- 930 Lampel, J., Friess, U. and Platt, U.: The impact of vibrational Raman scattering of air on DOAS measurements of
atmospheric trace gases, *Atmos. Meas. Tech.*, **8**, 3767–3787, doi :10.5194/amt-8-3767-2015, 2015.
- Lampel, J., Pöhler, D., Polyansky, O. L., Kyuberis, A. A., Zobov, N. F., Tennyson, J., Lodi, L., Frieß, U., Wang, Y., Beirle,
S., Platt, U., and Wagner, T.: Detection of water vapour absorption around 363 nm in measured atmospheric absorption
spectra and its effect on DOAS evaluations, *Atmos. Chem. Phys.*, **17**, 1271-1295, [https://doi.org/10.5194/acp-17-1271-
2017](https://doi.org/10.5194/acp-17-1271-2017), 2017
- 935 Li X., Brauers, T., Shao, M., Garland, R. M., Wagner, T., Deutschmann, T., and Wahner, A.: MAX-DOAS measurements in
southern China: retrieval of aerosol extinctions and validation using ground-based in-situ data. *Atmos. Chem. Phys.*, **10**,
2079–2089, 2010.
- Li, X., Brauers, T., Häsel, R., Bohn, B., Fuchs, H., Hofzumahaus, A., Holland, F., Lou, S., Lu, K.D., Rohrer, F. and Hu,
M.: Exploring the atmospheric chemistry of nitrous acid (HONO) at a rural site in Southern China, *Atmospheric
940 Chemistry and Physics*, **12**(3), 1497-1513, doi:10.5194/acp-12-1497-2012, 2012.
- Li, X., Brauers, T., Hofzumahaus, A., Lu, K., Li, Y. P., Shao, M., Wagner, T., and Wahner, A.: MAX-DOAS measurements
of NO₂, HCHO and CHOCHO at a rural site in Southern China, *Atmos. Chem. Phys.*, **13**, 2133-2151,
<https://doi.org/10.5194/acp-13-2133-2013>, 2013.
- 945 Li, X., Rohrer, F., Hofzumahaus, A., Brauers, T., Häsel, R., Bohn, B., Broch, S., Fuchs, H., Gomm, S., Holland, F. and
Jäger, J., Missing gas-phase source of HONO inferred from Zeppelin measurements in the troposphere, *Science*,
344(6181), 292-296, doi: 10.1126/science.1248999, 2014.
- Liu, M., Lin, J., Boersma, K. F., Pinardi, G., Wang, Y., Chimot, J., Wagner, T., Xie, P., Eskes, H., Van Roozendael, M.,
Hendrick, F., Wang, P., Wang, T., Yan, Y., Chen, L., and Ni, R.: Improved aerosol correction for OMI tropospheric
NO₂ retrieval over East Asia: constraint from CALIOP aerosol vertical profile, *Atmos. Meas. Tech.*, **12**, 1-21,
950 <https://doi.org/10.5194/amt-12-1-2019>, 2019.
- Ma, J. Z., Beirle, S., Jin, J. L., Shaiganfar, R., Yan, P., and Wagner, T.: Tropospheric NO₂ vertical column densities over
Beijing: results of the first three years of ground-based MAX-DOAS measurements (2008–2011) and satellite validation,
Atmos. Chem. Phys., **13**, 1547-1567, doi:10.5194/acp-13-1547-2013, 2013.
- Mayer, B. and Kylling, A.: Technical note: The libRadtran software package for radiative transfer calculations - description
955 and examples of use, *Atmos. Chem. Phys.*, **5**, 1855-1877, <https://doi.org/10.5194/acp-5-1855-2005>, 2005.
- Meller, R. and Moortgat, G. K.: Temperature dependence of the absorption cross sections of formaldehyde between 223 and
323 K in the wavelength range 225–375 nm, *J. Geophys. Res.*, **105**, 7089–7101, 2000



- 960 Monks, P.S., Granier, C., Fuzzi, S., Stohl, A., Williams, M.L., Akimoto, H., Amann, M., Baklanov, A., Baltensperger, U.,
Bey, I. and Blake, N.: Atmospheric composition change–global and regional air quality, *Atmospheric environment*,
43(33), 5268-5350, 2009.
- Nasse, J.-M., Eger, P. G., Pöhler, D., Schmitt, S., Frieß, U., and Platt, U.: Recent improvements of Long-Path DOAS
measurements: impact on accuracy and stability of short-term and automated long-term observations, *Atmos. Meas.*
Tech. Discuss., <https://doi.org/10.5194/amt-2019-69>, in review, 2019.
- 965 Neftel, A., Blatter, A., Hesterberg, R. and Staffelbach, T.: Measurements of concentration gradients of HNO₂ and HNO₃ over
a semi-natural ecosystem. *Atmospheric Environment*, 30(17), 3017-3025, doi: 10.1016/1352-2310(96)00011-8, 1996.
- Ortega, I., Coburn, S., Berg, L. K., Lantz, K., Michalsky, J., Ferrare, R. A., Hair, J. W., Hostetler, C. A., and Volkamer, R.:
The CU 2-D-MAX-DOAS instrument – Part 2: Raman scattering probability measurements and retrieval of aerosol
optical properties, *Atmos. Meas. Tech.*, 9, 3893-3910, doi:10.5194/amt-9-3893-2016, 2016.
- 970 Ortega, I., Koenig, T., Sinreich, R., Thomson, D., and Volkamer, R.: The CU 2-D-MAX-DOAS instrument – Part 1:
Retrieval of 3-D distributions of NO₂ and azimuth-dependent OVOC ratios, *Atmos. Meas. Tech.*, 8, 2371-2395,
doi:10.5194/amt-8-2371-2015, 2015.
- Pagsberg, P., E. Bjergbakke, E. Ratajczak, and Sillesen A.: Kinetics of the gas phase reaction OH + NO (+M) → O (+M) and
the determination of the UV absorption cross sections of HONO, *Chem. Phys. Lett.*, 272, 383-390, doi:10.1016/S0009-
2614(97)00576-9, 1997.
- 975 Peters, E., Pinardi, G., Seyler, A., Richter, A., Wittrock, F., Bösch, T., Van Roozendael, M., Hendrick, F., Drosoglou, T.,
Bais, A. F., Kanaya, Y., Zhao, X., Strong, K., Lampel, J., Volkamer, R., Koenig, T., Ortega, I., Puentedura, O., Navarro-
Comas, M., Gómez, L., Yela González, M., Pipers, A., Remmers, J., Wang, Y., Wagner, T., Wang, S., Saiz-Lopez, A.,
García-Nieto, D., Cuevas, C. A., Benavent, N., Querel, R., Johnston, P., Postlyakov, O., Borovski, A., Elokhov, A.,
Bruchkouski, I., Liu, H., Liu, C., Hong, Q., Rivera, C., Grutter, M., Stremme, W., Khokhar, M. F., Khayyam, J., and
980 Burrows, J. P.: Investigating differences in DOAS retrieval codes using MAD-CAT campaign data, *Atmos. Meas. Tech.*,
10, 955-978, <https://doi.org/10.5194/amt-10-955-2017>, 2017.
- Peters, E., Ostendorf, M., Bösch, T., Seyler, A., Schönhardt, A., Schreier, S. F., Henzing, J. S., Wittrock, F., Richter, A.,
Vrekoussis, M., and Burrows, J. P.: Full-azimuthal imaging-DOAS observations of NO₂ and O₄ during CINDI-2, *Atmos.*
Meas. Tech., 12, 4171–4190, <https://doi.org/10.5194/amt-12-4171-2019>, 2019.
- 985 Pinardi, G., Van Roozendael, M., Abuhassan, N., Adams, C., Cede, A., Clémer, K., Fayt, C., Frieß, U., Gil, M., Herman, J.,
Hermans, C., Hendrick, F., Irie, H., Merlaud, A., Navarro Comas, M., Peters, E., Pipers, A. J. M., Puentedura, O.,
Richter, A., Schönhardt, A., Shaiganfar, R., Spinei, E., Strong, K., Takashima, H., Vrekoussis, M., Wagner, T.,
Wittrock, F., and Yilmaz, S.: MAX-DOAS formaldehyde slant column measurements during CINDI: inter-comparison
and analysis improvement, *Atmos. Meas. Tech.*, 6, 167-185, doi:10.5194/amt-6-167-2013, 2013.
- 990 Pipers, A. J. M., Boersma, K. F., Kroon, M., Hains, J. C., Van Roozendael, M., Wittrock, F., Abuhassan, N., Adams, C.,
Akrami, M., Allaart, M. A. F., Apituley, A., Beirle, S., Bergwerff, J. B., Berkhout, A. J. C., Brunner, D., Cede, A.,
Chong, J., Clémer, K., Fayt, C., Frieß, U., Gast, L. F. L., Gil-Ojeda, M., Goutail, F., Graves, R., Griesfeller, A.,
Großmann, K., Hemerijckx, G., Hendrick, F., Henzing, B., Herman, J., Hermans, C., Hoexum, M., van der Hoff, G. R.,
Irie, H., Johnston, P. V., Kanaya, Y., Kim, Y. J., Klein Baltink, H., Kreher, K., de Leeuw, G., Leigh, R., Merlaud, A.,
995 Moerman, M. M., Monks, P. S., Mount, G. H., Navarro-Comas, M., Oetjen, H., Pazmino, A., Perez-Camacho, M.,
Peters, E., du Piesanie, A., Pinardi, G., Puentedura, O., Richter, A., Roscoe, H. K., Schönhardt, A., Schwarzenbach, B.,
Shaiganfar, R., Sluis, W., Spinei, E., Stolk, A. P., Strong, K., Swart, D. P. J., Takashima, H., Vlemmix, T., Vrekoussis,
M., Wagner, T., Whyte, C., Wilson, K. M., Yela, M., Yilmaz, S., Zieger, P., and Zhou, Y.: The Cabauw Inter-
comparison campaign for Nitrogen Dioxide measuring Instruments (CINDI): design, execution, and early results,
1000 *Atmos. Meas. Tech.*, 5, 457-485, doi:10.5194/amt-5-457-2012, 2012.



- Platt, U. and Stutz, J.: Differential Optical Absorption Spectroscopy. Springer-Verlag Heidelberg, Berlin, 229-375, 2008.
- Polyansky, O. L., Kyuberis, A. A., Lodi, L., Tennyson, J., Ovsyannikov, R. I., and Zobov, N.: ExoMol molecular line lists XX: high accuracy computed line list for hot H₂¹⁶O, *Mon. Not. R. Astron. Soc.*, 2016.
- 1005 Puķīte, J., Kühn, S., Deutschmann, T., Platt, U. and Wagner, T.: Extending differential optical absorption spectroscopy for limb measurements in the UV, *Atmospheric Measurement Techniques*, 3(3), 631-653, doi:10.5194/amt-3-631-2010, 2010.
- Rodgers, C. D.: Inverse methods for atmospheric sounding, theory and practice, Series on Atmospheric, Oceanic and Planetary Physics, World Scientific, 2000.
- 1010 Rohrer, F., Bohn, B., Brauers, T., Brüning, D., Johnen, F.-J., Wahner, A., and Kleffmann, J.: Characterisation of the photolytic HONO-source in the atmosphere simulation chamber SAPHIR, *Atmos. Chem. Phys.*, 5, 2189-2201, doi:10.5194/acp-5-2189-2005, 2005.
- Roscoe, H. K., Van Roozendaal, M., Fayt, C., du Piesanie, A., Abuhassan, N., Adams, C., Akrami, M., Cede, A., Chong, J., Clémer, K., Friess, U., Gil Ojeda, M., Goutail, F., Graves, R., Griesfeller, A., Grossmann, K., Hemerijckx, G., Hendrick, F., Herman, J., Hermans, C., Irie, H., Johnston, P. V., Kanaya, Y., Kreher, K., Leigh, R., Merlaud, A., Mount, G. H., 1015 Navarro, M., Oetjen, H., Pazmino, A., Perez-Camacho, M., Peters, E., Pinardi, G., Puentedura, O., Richter, A., Schönhardt, A., Shaiganfar, R., Spinei, E., Strong, K., Takashima, H., Vlemmix, T., Vrekoussis, M., Wagner, T., Wittrock, F., Yela, M., Yilmaz, S., Boersma, F., Hains, J., Kroon, M., Piders, A., and Kim, Y. J.: Inter-comparison of slant column measurements of NO₂ and O₄ by MAX-DOAS and zenith-sky UV and visible spectrometers, *Atmos. Meas. Tech.*, 3, 1629-1646, doi:10.5194/amt-3-1629-2010, 2010.
- 1020 Rozanov, A., Rozanov, V., Buchwitz, M., Kokhanovsky, A., and Burrows, J.: SCIATRAN 2.0 - A new radiative transfer model for geophysical applications in the 175-2400 nm spectral region, in: *Atmospheric Remote Sensing: Earth's Surface, Troposphere, Stratosphere and Mesosphere - I*, edited by Burrows, J. and Eichmann, K., vol. 36 of *ADVANCES IN SPACE RESEARCH*, 1015-1019, 2005.
- 1025 Rozanov, V.V., Rozanov, A.V., Kokhanovsky, A.A. and Burrows, J.P.: Radiative transfer through terrestrial atmosphere and ocean: software package SCIATRAN. *Journal of Quantitative Spectroscopy and Radiative Transfer*, 133, 13-71, 2014.
- Ryan, R. G., Rhodes, S., Tully, M., Wilson, S., Jones, N., Frieß, U., and Schofield, R.: Daytime HONO, NO₂ and aerosol distributions from MAX-DOAS observations in Melbourne, *Atmos. Chem. Phys.*, 18, 13969-13985, <https://doi.org/10.5194/acp-18-13969-2018>, 2018.
- 1030 Spurr, R.: LIDORT and VLIDORT: Linearized pseudo-spherical scalar and vector discrete ordinate radiative transfer models for use in remote sensing retrieval problems, *Light Scattering Reviews*, Volume 3, edited by: Kokhanovsky, A., Springer, 2008.
- Spurr, R.: User's Guide VLIDORT Version 2.6, RT Solutions, Inc., 2013
- 1035 Sörgel, M., Regelin, E., Bozem, H., Diesch, J.-M., Drewnick, F., Fischer, H., Harder, H., Held, A., Hosaynali-Beygi, Z., Martinez, M., and Zetzsch, C.: Quantification of the unknown HONO daytime source and its relation to NO₂, *Atmos. Chem. Phys.*, 11, 10433-10447, doi:10.5194/acp-11-10433-2011, 2011.
- Stuhl, F. and Niki H.: Flash photochemical study of the reaction OH + NO + M using resonance fluorescent detection of OH, *J. Chem. Phys.*, 57, 3677-3679, doi:10.1063/1.1678826, 1972.
- 1040 Stutz, J., Kim, E. S., Platt, U., Bruno, P., Perrino, C., and Febo, A.: UV-vis Absorption Cross-Section of Nitrous Acid, *J. Geophys. Res.*, 105, 14585-14592, 2000.
- Su, H., Cheng, Y., Oswald, R., Behrendt, T., Trebs, I., Meixner, F.X., Andreae, M.O., Cheng, P., Zhang, Y. and Pöschl, U.: Soil nitrite as a source of atmospheric HONO and OH radicals, *Science*, 333(6049), 1616-1618, doi:10.1126/science.1207687, 2011.



- 1045 Su, H., Cheng, Y.F., Shao, M., Gao, D.F., Yu, Z.Y., Zeng, L.M., Slanina, J., Zhang, Y.H. and Wiedensohler, A.: Nitrous acid (HONO) and its daytime sources at a rural site during the 2004 PRIDE - PRD experiment in China. *Journal of Geophysical Research: Atmospheres*, 113(D14), doi: 10.1029/2007JD009060, 2008.
- Serduchenko, A., Gorshchev, V., Weber, M., Chehade, W. and Burrows, J.P.: High spectral resolution ozone absorption cross-sections—Part 2: Temperature dependence. *Atmospheric Measurement Techniques*, 7(2), 625–636, 2014.
- 1050 Thalman, R. M. and Volkamer, R.: Temperature Dependent Absorption Cross-Sections of O₂-O₂ collision pairs between 340 and 630 nm and at atmospherically relevant pressure, *Phys. Chem. Chem. Phys.*, 15, 15371–15381, doi:10.1039/c3cp50968k, 2013.
- 1055 Tirpitz, J.-L., Frieß, U., Hendrick, F., Alberti, C., Allaart, M., Apituley, A., Bais, A., Beirle, S., Berkhout, S., Bognar, K., Bösch, T., Bruchkouski, I., Cede, A., Chan, K. L., den Hoed, M., Donner, S., Drosoglou, T., Fayt, C., Friedrich, M. M., Frumau, A., Gast, L., Gielen, C., Gomez-Martín, L., Hao, N., Hensen, A., Henzing, B., Hermans, C., Jin, J., Kreher, K., Kuhn, J., Lampel, J., Li, A., Liu, C., Liu, H., Ma, J., Merlaud, A., Peters, E., Pinardi, G., Piders, A., Platt, U., Puentedura, O., Richter, A., Schmitt, S., Spinei, E., Stein Zweers, D., Strong, K., Swart, D., Tack, F., Tiefengraber, M., van der Hoff, R., van Roozendael, M., Vlemmix, T., Vonk, J., Wagner, T., Wang, Y., Wang, Z., Wenig, M., Wiegner, M., Wittrock, F., Xie, P., Xing, C., Xu, J., Yela, M., Zhang, C., and Zhao, X.: Intercomparison of MAX-DOAS vertical profile retrieval algorithms: studies on field data from the CINDI-2 campaign, *Atmos. Meas. Tech. Discuss.*, https://doi.org/10.5194/amt-2019-456, in review, 2020.
- 1060 Van Roozendael, M., Fayt, C., Post, P., Hermans, C., Lambert, J.-C.: Retrieval of BrO and NO₂ from UV-Visible Observations, in: *Sounding the troposphere from space: a new Era for Atmospheric Chemistry. The TROPOSAT Final Report*. Peter Borrell, Patricia M. Borrell, John P. Burrows and Ulrich Platt (editors), Springer Verlag, 155–166, 2003
- 1065 Vandaele, A. C., Hermans, C., Simon, P. C., Carleer, M., Colin, R., Fally, S., Mérienne, M.-F., Jenouvrier, A., and Coquart, B.: Measurements of the NO₂ absorption cross section from 42000 cm⁻¹ to 10000 cm⁻¹ (238–1000 nm) at 220 K and 294 K, *J. Quant. Spectrosc. Ra.*, 59, 171–184, 1998.
- Vlemmix, T., Piders, A. J. M., Stammes, P., Wang, P., and Levelt, P. F.: Retrieval of tropospheric NO₂ using the MAX-DOAS method combined with relative intensity measurements for aerosol correction, *Atmos. Meas. Tech.*, 3, 1287–1305, 2010.
- 1070 Vlemmix, T., Piders, A. J. M., Berkhout, A. J. C., Gast, L. F. L., Wang, P., and Levelt, P. F.: Ability of the MAX-DOAS method to derive profile information for NO₂: can the boundary layer and free troposphere be separated?, *Atmos. Meas. Tech.*, 4, 2659–2684, 2011
- Vlemmix, T., Hendrick, F., Pinardi, G., De Smedt, I., Fayt, C., Hermans, C., Piders, A., Wang, P., Levelt, P., and Van Roozendael, M.: MAXDOAS observations of aerosols, formaldehyde and nitrogen dioxide in the Beijing area: comparison of two profile retrieval approaches, *Atmos. Meas. Tech.*, 8, 941–963, doi:10.5194/amt-8-941-2015, 2015.
- 1075 Wagner, T., B. Dix, C. von Friedeburg, Frieß, U., Sanghavi, S., Sinreich, R. and Platt, U.: MAX-DOAS O₄ measurements: A new technique to derive information on atmospheric aerosols—Principles and information content, *J. Geophys. Res.*, 109, D22205, 2004.
- 1080 Wagner, T., Beirle, S., and Deutschmann, T.: Three-dimensional simulation of the Ring effect in observations of scattered sun light using Monte Carlo radiative transfer models, *Atmos. Meas. Tech.*, 2, 113–124, 2009.
- Wagner, T., Beirle, S., Brauers, T., Deutschmann, T., Frieß, U., Hak, C., Halla, J. D., Heue, K. P., Junkermann, W., Li, X., Platt, U. and Pundt-Gruber, I.: Inversion of tropospheric profiles of aerosol extinction and HCHO and NO₂ mixing ratios from MAX-DOAS observations in Milano during the summer of 2003 and comparison with independent data sets, *Atmos. Meas. Tech. Discuss.*, 4, 3891–3964, 2011.
- 1085 Wagner, T., Beirle, S., Dörner, S., Friess, U., Remmers, J. and Shaiganfar, R.: Cloud detection and classification based on MAX-DOAS observations, *Atmos. Meas. Tech.*, 7, 1289–1320, 2014



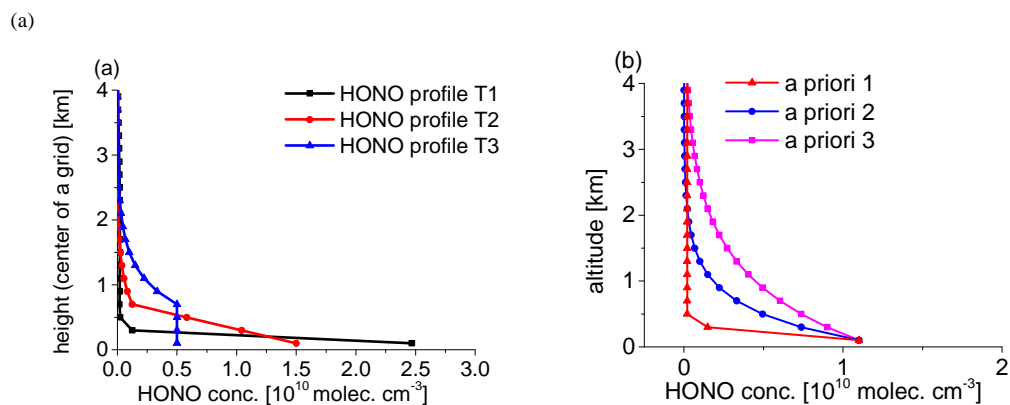
- Wagner, T., Beirle, S., Remmers, J., Shaiganfar, R., and Wang, Y.: Absolute calibration of the colour index and O₄ absorption derived from Multi AXis (MAX-)DOAS measurements and their application to a standardised cloud classification algorithm, *Atmos. Meas. Tech.*, 9, 4803-4823, <https://doi.org/10.5194/amt-9-4803-2016>, 2016.
- 1090 Wang, Y., Li, A., Xie, P. H., Chen, H., Xu, J., Wu, F. C., G., L. J., and Q., L. W.: Retrieving vertical profile of aerosol extinction by multi-axis differential optical absorption spectroscopy, *Acta Phys. Sin.*, 16, doi: 10.7498/aps.62.180705, <http://wulixb.iphys.ac.cn/EN/abstract/abstract54703.shtml#>, 2013a.
- Wang, Y., Li, A., Xie, P. H., Chen, H., Mou, F. S., Xu, J., Wu, F. C., Zeng, Y., Liu, J. G. and Liu, W. Q.: Measuring tropospheric vertical distribution and vertical column density of NO₂ by multi-axis differential optical absorption spectroscopy, *Acta Phys. Sin.*, 16, DOI:10.7498/aps.62.200705, <http://wulixb.iphys.ac.cn/EN/abstract/abstract56201.shtml>, 2013b.
- 1095 Wang, Y., Li, A., Xie, P. H., Wagner, T., Chen, H., Liu, W. Q., and Liu, J. G.: A rapid method to derive horizontal distributions of trace gases and aerosols near the surface using multi-axis differential optical absorption spectroscopy, *Atmos. Meas. Tech.*, 7, 1663-1680, doi:10.5194/amt-7-1663-2014, 2014.
- 1100 Wang, Y., Penning de Vries, M., Xie, P. H., Beirle, S., Dörner, S., Remmers, J., Li, A., and Wagner, T.: Cloud and aerosol classification for 2.5 years of MAX-DOAS observations in Wuxi (China) and comparison to independent data sets, *Atmos. Meas. Tech.*, 8, 5133-5156, doi:10.5194/amt-8-5133-2015, 2015.
- Wang, Y., Beirle, S., Lampel, J., Koukouli, M., De Smedt, I., Theys, N., Ang, L., Wu, D., Xie, P., Liu, C. and Van Roozendael, M.: Validation of OMI, GOME-2A and GOME-2B tropospheric NO₂, SO₂ and HCHO products using MAX-DOAS observations from 2011 to 2014 in Wuxi, China: investigation of the effects of priori profiles and aerosols on the satellite products. *Atmospheric Chemistry and Physics*, 17(8), p.5007, 2017a.
- 1105 Wang, Y., Lampel, J., Xie, P., Beirle, S., Li, A., Wu, D., and Wagner, T.: Ground-based MAX-DOAS observations of tropospheric aerosols, NO₂, SO₂ and HCHO in Wuxi, China, from 2011 to 2014, *Atmos. Chem. Phys.*, 17, 2189-2215, <https://doi.org/10.5194/acp-17-2189-2017>, 2017b.
- 1110 Wang, Y., Beirle, S., Hendrick, F., Hilboll, A., Jin, J., Kyuberis, A. A., Lampel, J., Li, A., Luo, Y., Lodi, L., Ma, J., Navarro, M., Ortega, I., Peters, E., Polyansky, O. L., Remmers, J., Richter, A., Puentedura, O., Van Roozendael, M., Seyler, A., Tennyson, J., Volkamer, R., Xie, P., Zobov, N. F., and Wagner, T.: MAX-DOAS measurements of HONO slant column densities during the MAD-CAT campaign: inter-comparison, sensitivity studies on spectral analysis settings, and error budget, *Atmos. Meas. Tech.*, 10, 3719-3742, <https://doi.org/10.5194/amt-10-3719-2017>, 2017c.
- 1115 Wang, Y., Dörner, S., Donner, S., Böhnke, S., De Smedt, I., Dickerson, R. R., Dong, Z., He, H., Li, Z., Li, Z., Li, D., Liu, D., Ren, X., Theys, N., Wang, Y., Wang, Y., Wang, Z., Xu, H., Xu, J., and Wagner, T.: Vertical profiles of NO₂, SO₂, HONO, HCHO, CHOCHO, and aerosols derived from MAX-DOAS measurements at a rural site in the central-western North China Plain and their relation to emission sources and effects of regional transport, *Atmos. Chem. Phys. Discuss.*, <https://doi.org/10.5194/acp-2018-1137>, in review, 2018a.
- 1120 Wang, Y., Puķīte, J., Wagner, T., Donner, S., Beirle, S., Hilboll, A., Vrekoussis, M., Richter, A., Apituley, A., PETERS, A. and Allaart, M.: Vertical Profiles of Tropospheric Ozone From MAX-DOAS Measurements During the CINDI-2 Campaign: Part 1—Development of a New Retrieval Algorithm, *Journal of Geophysical Research: Atmospheres*, 123(18), pp.10-637, 2018b.
- 1125 Wittrock, F., Oetjen, H., Richter, A., Fietkau, S., Medeke, T., Rozanov, A., and Burrows, J. P.: MAX-DOAS measurements of atmospheric trace gases in Ny-Alesund – Radiative transfer studies and their application, *Atmos. Chem. Phys.*, 4, 955–966, 2004.
- Wittrock, F.: The Retrieval of Oxygenated Volatile Organic Compounds by Remote Sensing Techniques. Ph.D., University of Bremen, Bremen, Germany, 2006, Available at: http://www.doas-bremen.de/paper/diss_wittrock_06.pdf (last accessed December 2015).



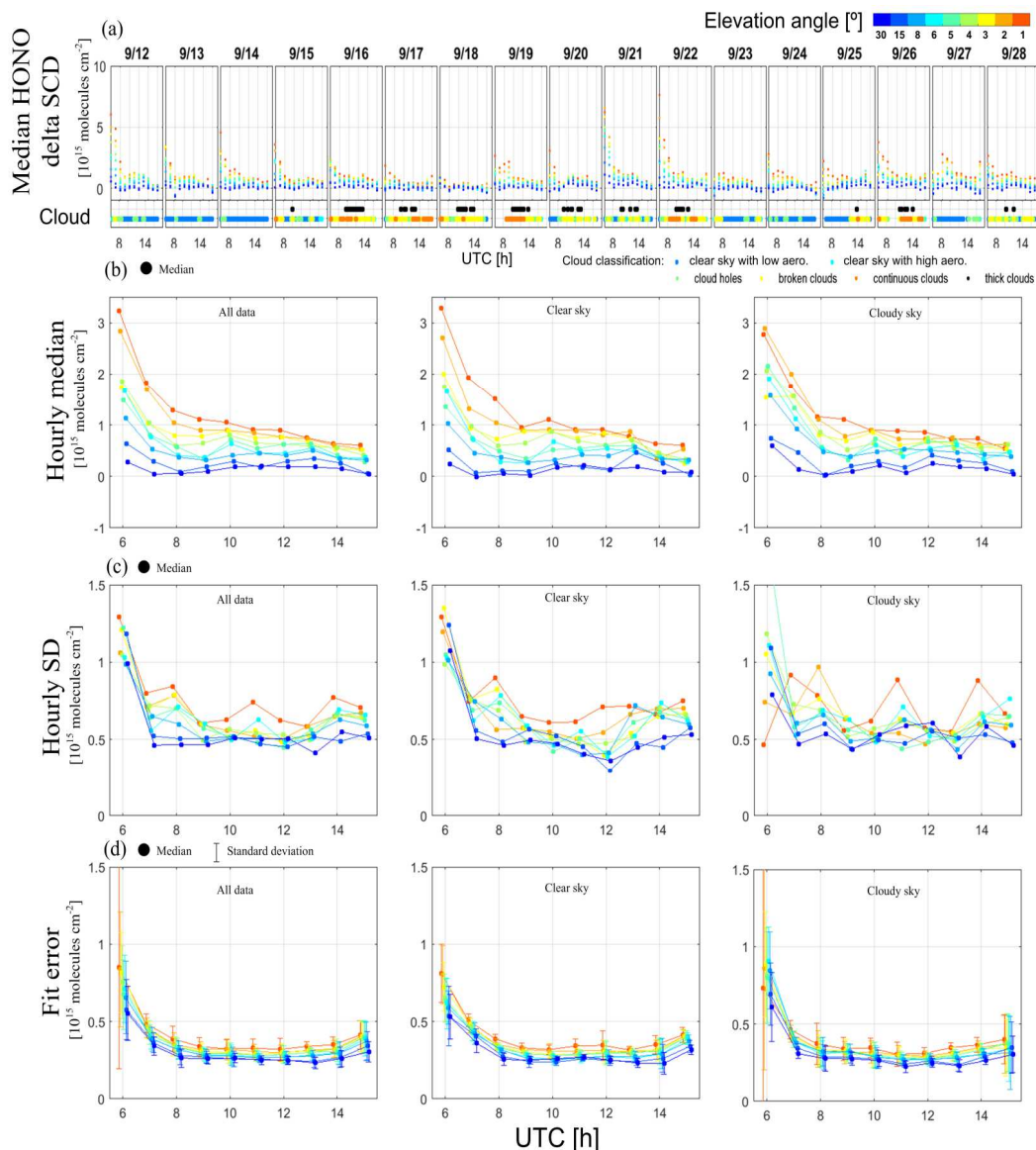
- 1130 Wong, K. W., Tsai, C., Lefer, B., Haman, C., Grossberg, N., Brune, W. H., Ren, X., Luke, W., and Stutz, J.: Daytime HONO Vertical gradients during SHARP 2009 in Houston, TX, *Atmos. Chem. Phys.*, 12, 635–652, doi:10.5194/acp-12-635-2012, 2012.
- Yilmaz, S.: Retrieval of Atmospheric Aerosol and Trace Gas Vertical Profiles using Multi-Axis Differential Optical Absorption Spectroscopy, PhD thesis, University of Heidelberg, Germany, 2012.
- 1135 Zieger, P., Weingartner, E., Henzing, J., Moerman, M., de Leeuw, G., Mikkilä, J., Ehn, M., Petäjä, T., Clémer, K., van Roozendaal, M., Yilmaz, S., Frieß, U., Irie, H., Wagner, T., Shaiganfar, R., Beirle, S., Apituley, A., Wilson, K., and Baltensperger, U.: Comparison of ambient aerosol extinction coefficients obtained from in-situ, MAX-DOAS and LIDAR measurements at Cabauw, *Atmos. Chem. Phys.*, 11, 2603–2624, doi:10.5194/acp-11-2603-2011, 2011.



1140 **Figures**



1145 **Figure 1:** (a) Assumed HONO profiles used for the RTM simulations of the HONO delta SCDs. (b) Three different a priori profiles which were used for the sensitivity studies based on synthetic HONO delta SCDs.



1150 **Figure 2:** Overview of the HONO delta SCDs retrieved from all MAX-DOAS instruments using the “sequential FRS” during the whole CINDI-2 campaign period. (a) Time series of median HONO delta SCDs derived from measurements of all MAX-DOAS instruments by individual groups. The results of the cloud classification algorithm (applied to the “MPIC” measurements) are shown at the bottom of the subfigures. The colours indicate the elevation angles and cloud categories, respectively. The colours in (b), (c), and (d) indicate elevation angles as shown in the upper panel of (a). (b) Diurnal variations of hourly median HONO delta SCDs derived from all MAX-DOAS instruments. (c) Diurnal variation of hourly standard deviations of differences from median HONO delta SCDs from all MAX-DOAS instruments. (d) Hourly median and standard deviations of the DOAS fit errors of the HONO delta SCDs from all MAX-DOAS instruments. The left, centre, and right columns of subfigures represent the results for all the data, as well as results for “clear sky”, and “cloudy sky” conditions, respectively.

1155

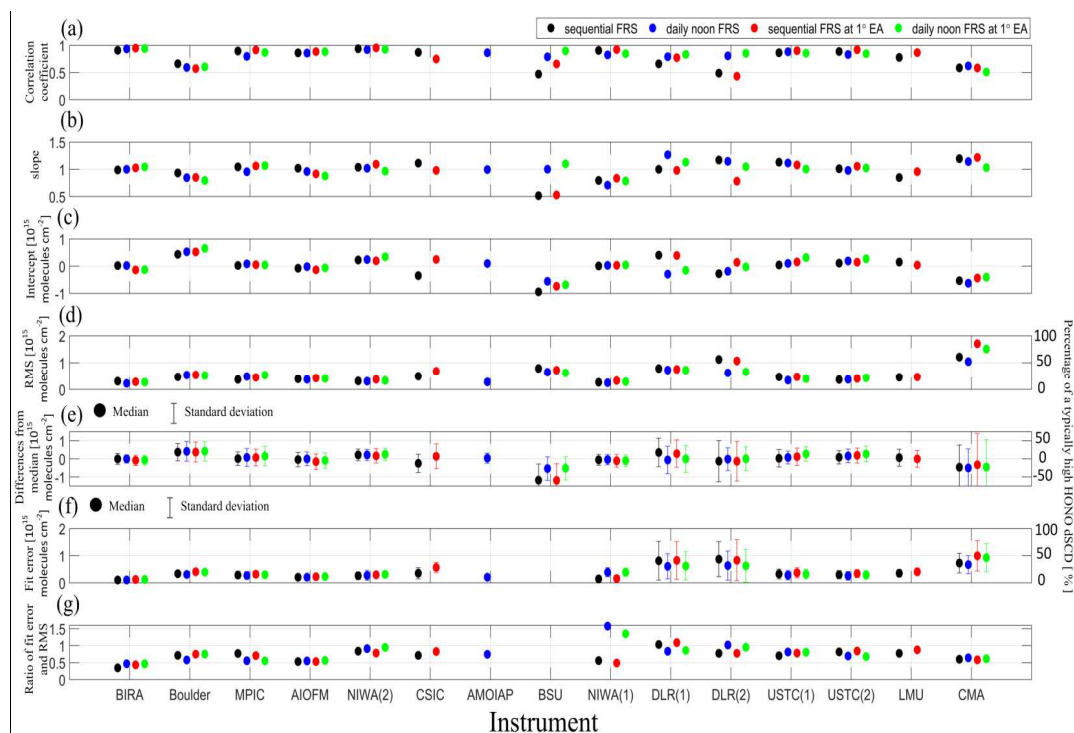
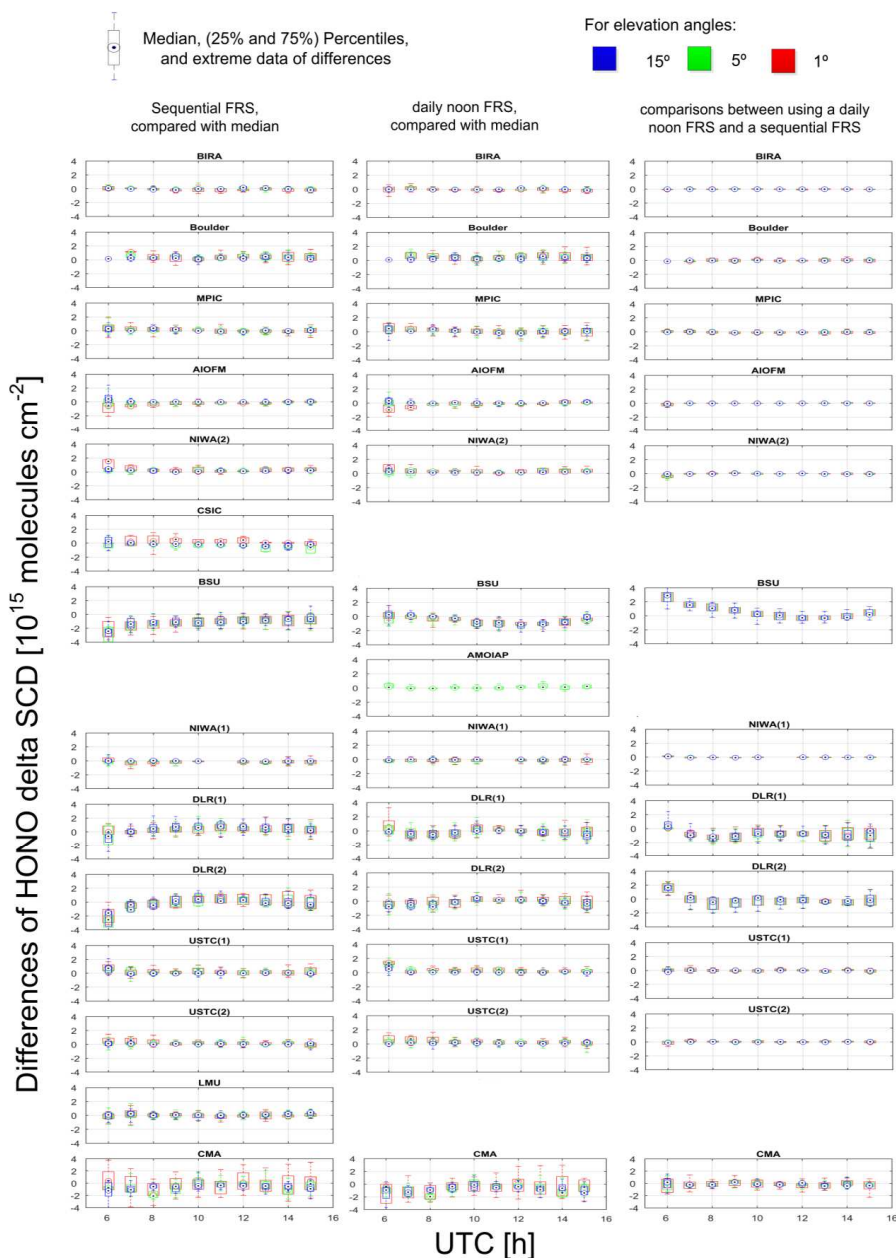
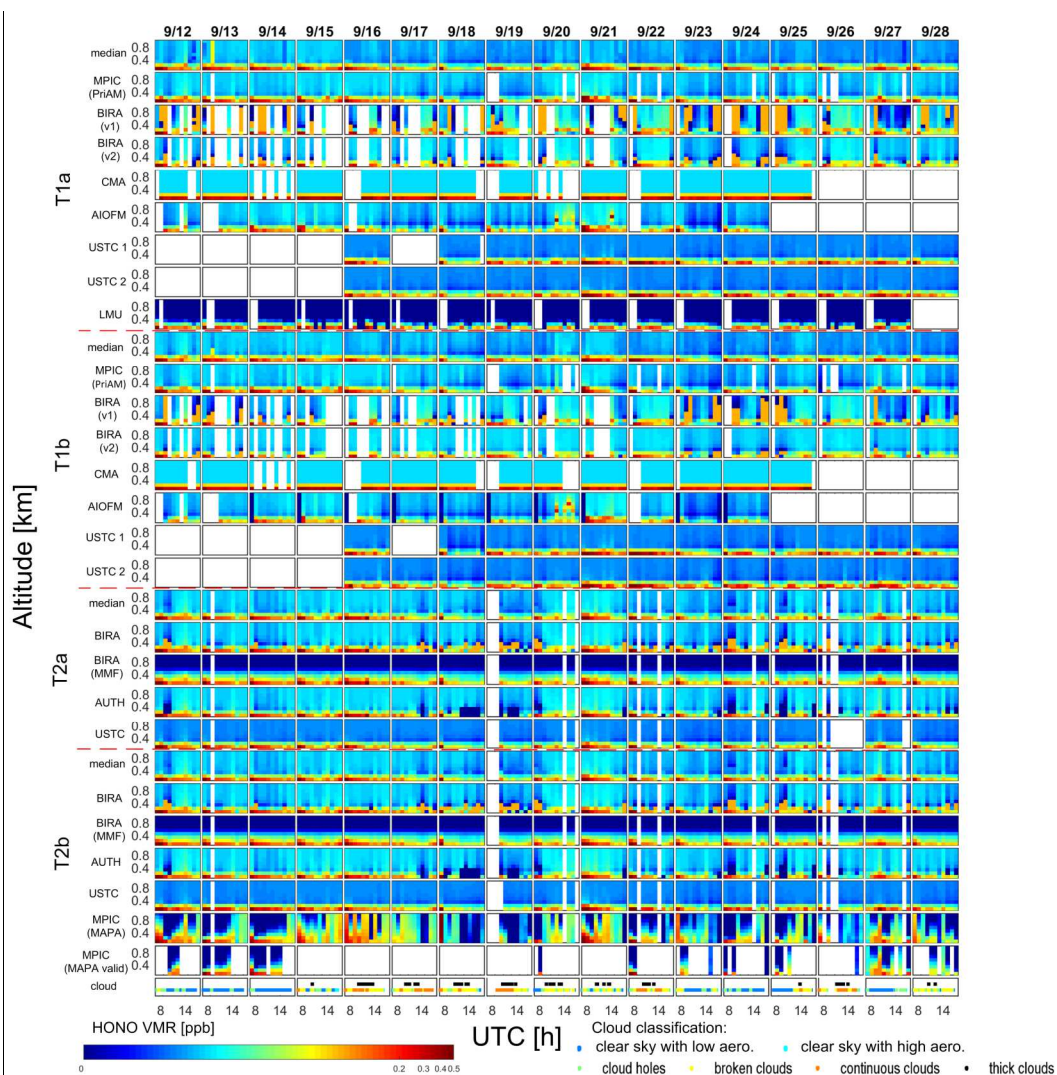


Figure 3: Correlation coefficients (a), slopes (b), intercepts (c), and RMS of the residuals (d) derived from the linear regressions versus the median values. The median differences and standard deviations derived from the comparison of the HONO delta SCDs from individual instruments and the median values of all instruments during the whole CINDI-2 campaign period are shown in (e). In (f) the median values and the standard deviation of the DOAS fit error are shown. The y axis on the right side of (d), (e), and (f) indicate percentages calculated by dividing the absolute errors by a typical high HONO delta SCD of 2×10^{15} molecules cm^{-2} . In (g) ratios of RMS and DOAS fit errors are shown.

1160

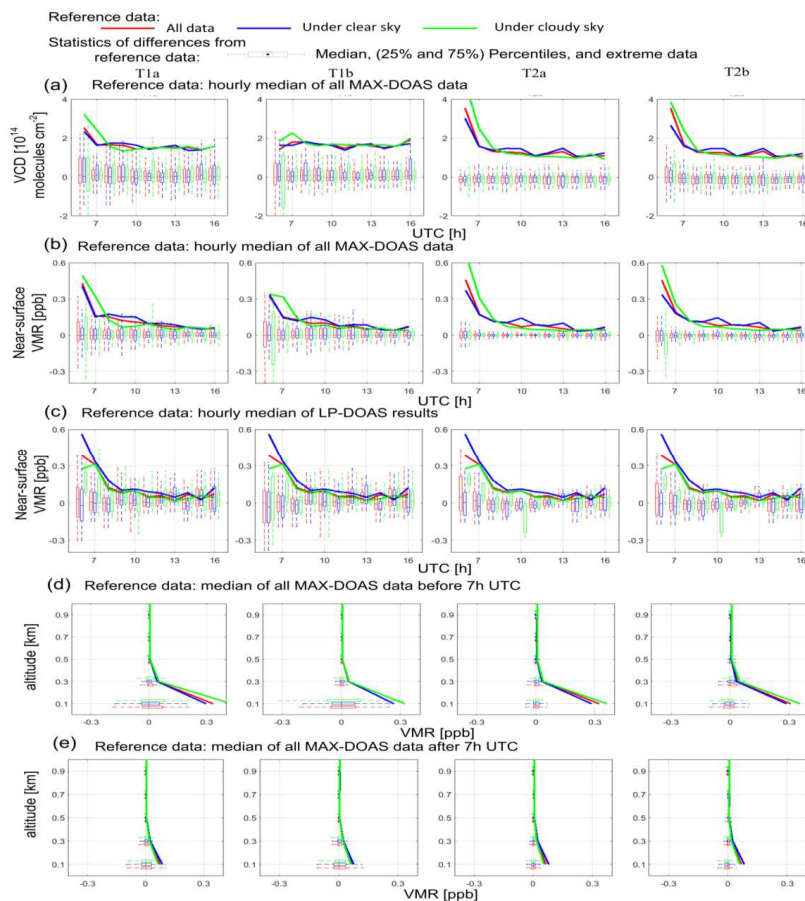


1165 **Figure 4:** Boxplots (including median, percentiles, and extreme data) of the differences of the HONO delta SCDs for individual instruments (one instrument each row) with respect to the median values for the results using a “sequential FRS” (the left column) or a “daily noon FRS” (the middle column). In the right column of subplots, the differences of the HONO delta SCDs for the results using a “sequential FRS” or “daily noon FRS” are shown in for the individual instruments. Colours indicate the elevation angles. The gaps between the subplots are due to unavailability of the corresponding data.



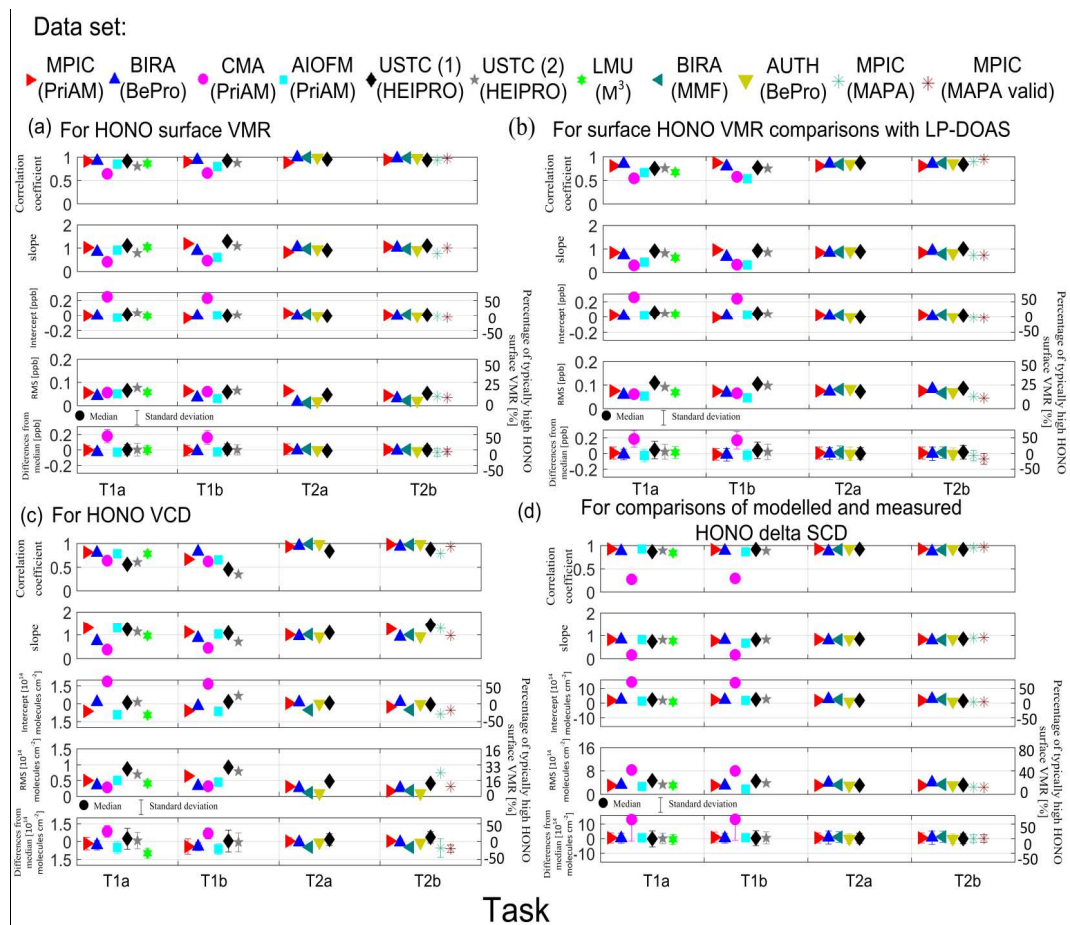
1170

Figure 5: Overview of the time series of HONO profiles derived by different institutes and instruments for the four tasks. The median values for the individual tasks are also given. The colormap is given in logarithmic scale in order to show fine structures of low HONO VMR values above the surface. The cloud classification results are shown in the small subfigures at the bottom.

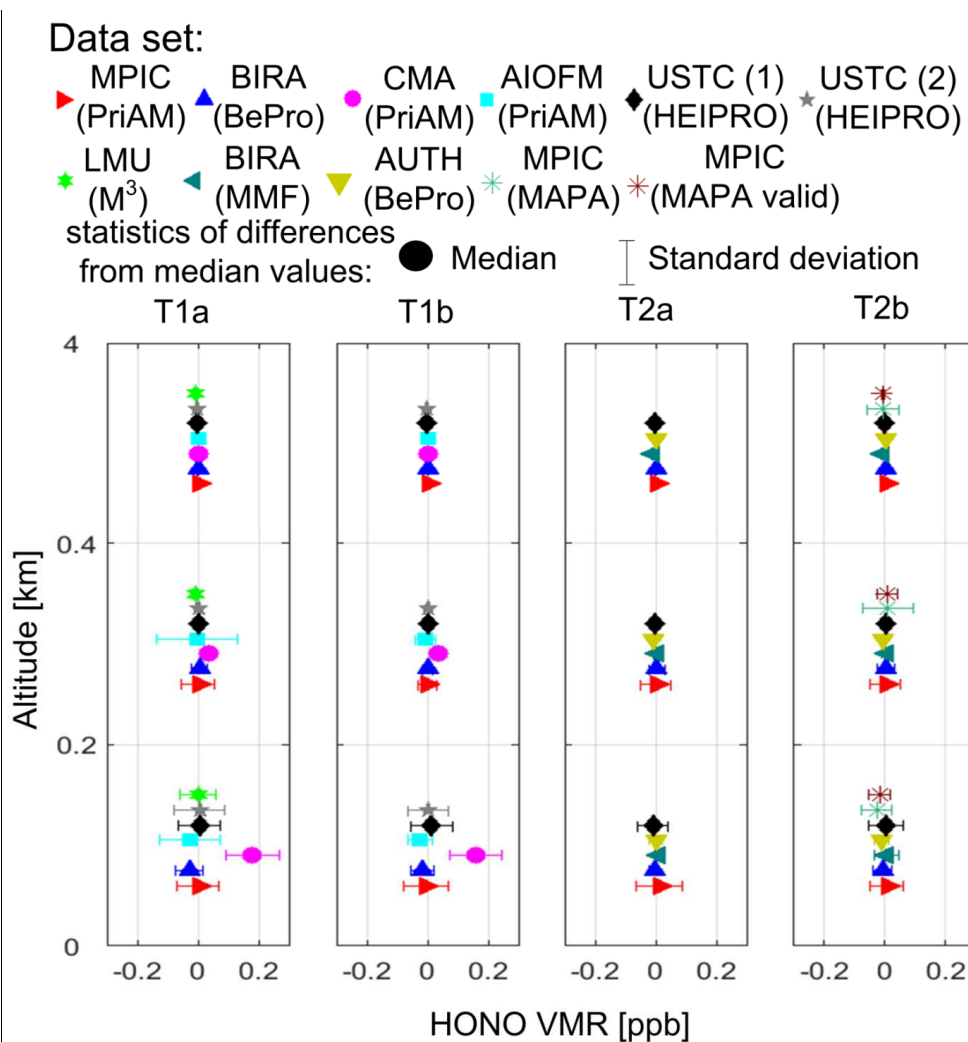


1175 **Figure 6:** Boxplots of the differences of the HONO VCDs (a), near-surface VMRs (b), profiles before (d) and after 7 UTC (e) derived by different institutes compared to the median values for the whole campaign. Boxplots of the differences of the HONO near-surface VMRs compared to the co-located LP-DOAS measurements are shown in (c). Colours in all subfigures indicate the sky condition. Comparisons of data sets for the four tasks are shown in the different columns of subfigures. Comparison results are calculated for different hours during the day in (a), (b), and (c). The reference values for the comparisons are also given by the solid lines in each subfigure. The reference values are hourly median of HONO VCDs (a), near-surface VMRs (b), and profiles before (d) and after 7 UTC (e) derived from all MAX-DOAS data, and near-surface VMRs derived from the co-located LP-DOAS measurements (c), respectively.

1180



1185 **Figure 7: Correlation coefficients, slopes, intercepts, and RMS of the residuals of the linear regression as well as median differences between individual participants and the reference values, which are the median values of all MAX-DOAS (a), (c), and of the co-located LP-DOAS measurements (b). Comparisons of the near-surface HONO VMRs are given in (a) and (b). Comparisons of HONO VCDs are given in (c). For the individual data sets, the same comparison parameters are derived for the comparison of measured and modelled HONO delta SCDs (d).**



1190

Figure 8: Median and standard deviations of the differences of the HONO VMR profiles derived from the individual participants compared to median values of all MAX-DOAS data for the whole campaign. The results in the vertical grids of 0 km to 0.2 km, 0.2 km to 0.4 km, and 0.4 km to 4 km are shown as three vertical clusters of dots in the figures. Different subfigures represent results for different tasks.

1195

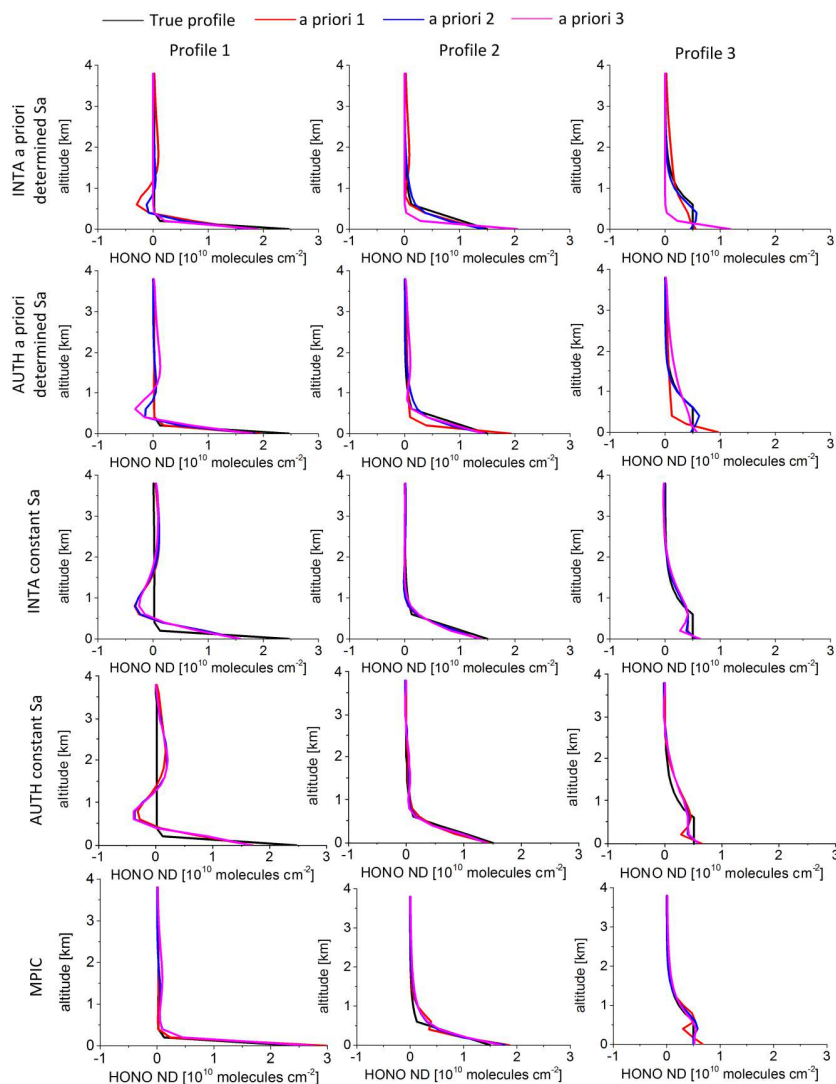
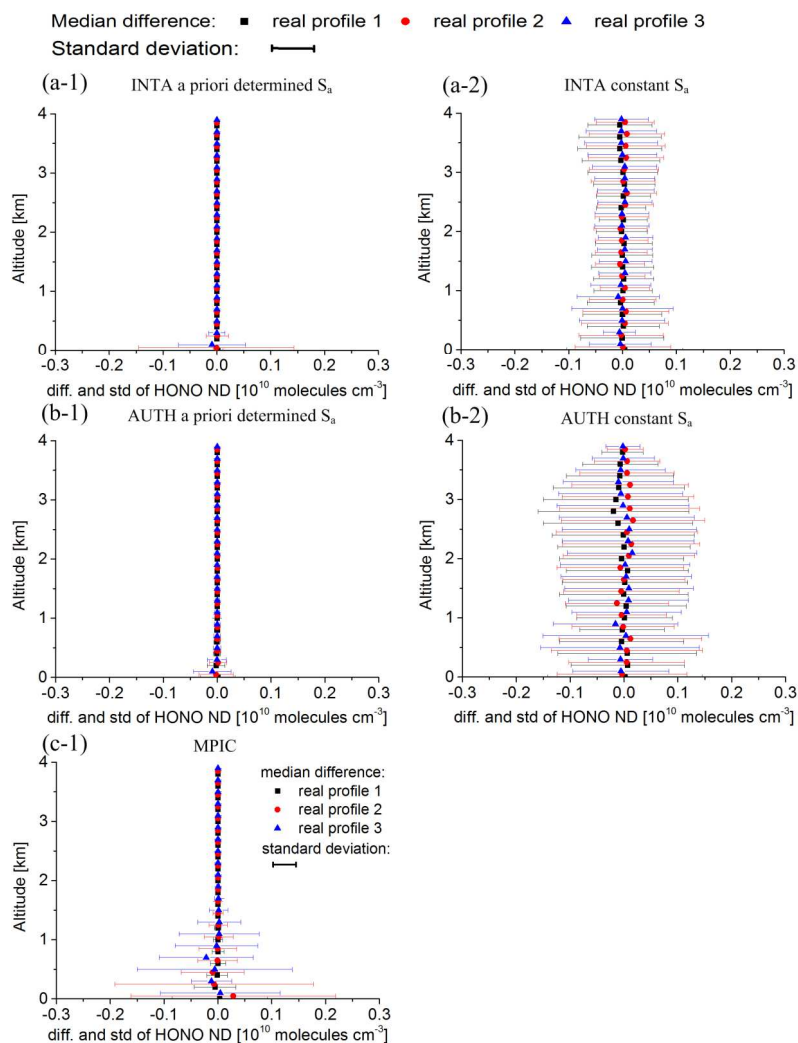
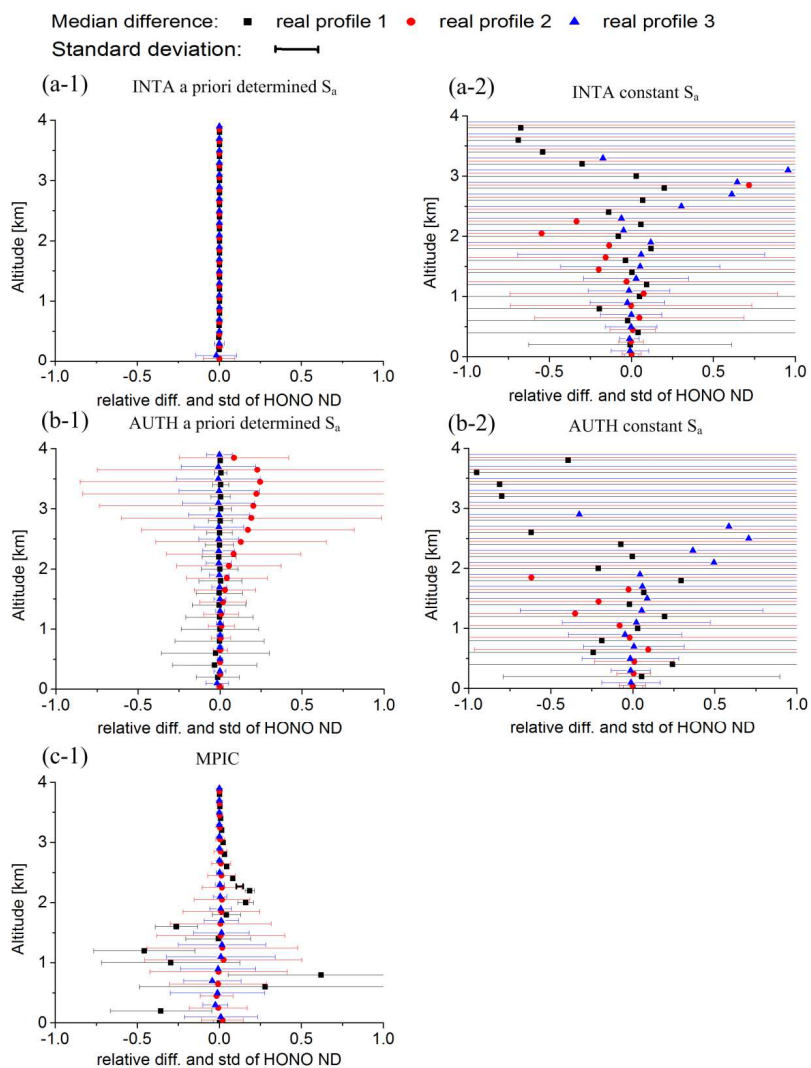


Figure 9: HONO profiles retrieved from simulated HONO delta SCDs by the different participants using different inversion algorithm with “constant Sa” and “a priori determined Sa” (see text). The black curves in the different columns of the figure indicate the different input profiles, the other colours indicate the profiles retrieved using different a priori profiles (see Fig. 1b).



1200

Figure 10: Median and standard deviations of the differences of the HONO VMR profiles retrieved from the simulated HONO delta SCDs with added artificial noise compared to those without noise by the different participants using different inversion algorithm with “constant S_a ” and “a priori determined S_a ” (see text). The root mean square of the noise is 3×10^{14} molecules cm^{-2} . The different colours indicate the results for the three different assumed HONO profiles.

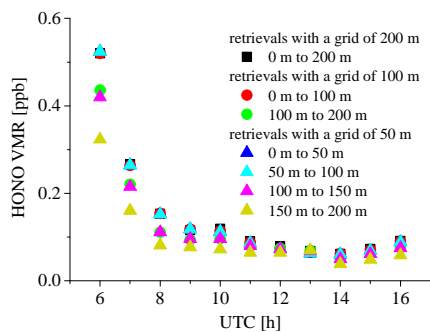


1205

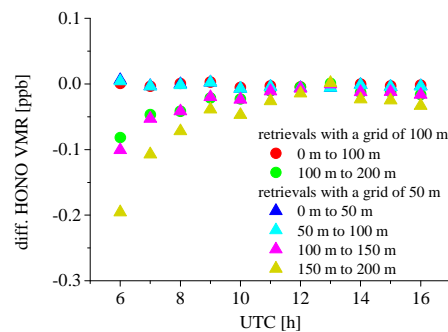
Figure 11: Median and standard deviations of the relative differences of the HONO VMR profiles retrieved from the simulated HONO delta SCDs with added artificial noise compared to those without noise by the different participants using different inversion algorithm with “constant S_a ” and “a priori determined S_a ” (see text).



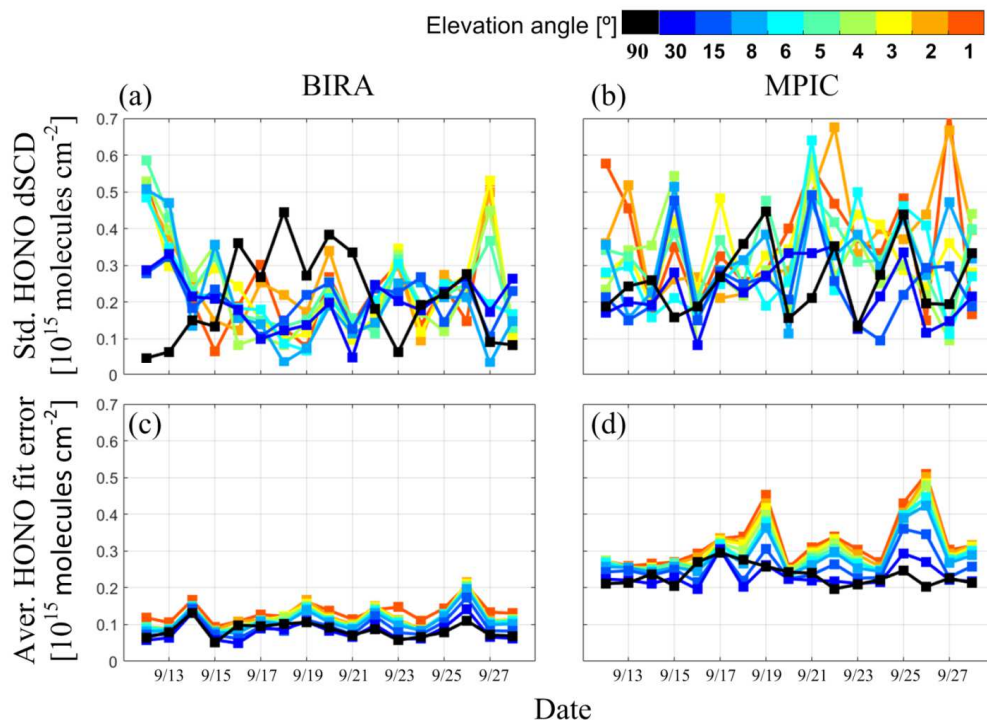
1210 (a)



(b)



1215 **Figure 12:** (a) Averaged diurnal variations of the HONO VMRs in the altitude range of up to 200 m retrieved using the “PriAM” algorithm using vertical grid intervals of 50 m, 100 m and 200 m, respectively. Note that the results in the altitude grids below 200 m are given respectively. The results are derived from the HONO delta SCD measured by the MPIC instrument. (b) Averaged diurnal variations of the differences of the HONO VMRs retrieved for vertical grid intervals of 50 m, and 100 m compared to those retrieved for the vertical grid interval of 200 m.



1220 **Figure 13:** Standard deviations (top panel) and averaged DOAS fit errors (bottom panel) of HONO dSCDs retrieved using the daily noon FRS in the time period of 11 to 16 UTC for individual days for the BIRA (left panel) and the MPIC (right panel) instruments, respectively. The colormap indicates elevation angles.



Tables

Table 1 Overview on instrumental properties and analysis software used by the different participants

Institute	CINDI-2 Instrument ID*	Instrument type	Spectral range (nm)	Spectral Res. (nm)	Detector T [°C]	Field of view (° FWHM)	Fit software	dSCD inter-comparison task		Profile inversion algorithm	profile inter-comparison task				Synthetic analysis
								Sequential FRS	Daily FRS		T1a	T1b	T2a	T2b	
BIRA ^a	bira-4	in-house developed 2D	300-390	0.37	-50	0.5	QDOAS	×	×	BePro	×	×	×	×	-
										MMF	-	-	×	×	
Boulder ^b	cu-boulder-11	in-house developed 2D	325-470	0.7	-30	0.7	QDOAS	×	×	-	-	-	-	-	-
MPIC ^c	mpic-28	in-house developed 1D	315-475	0.72	20	1	QDOAS	×	×	PriAM	×	×	×	×	×
										MAPA	-	-	-	×	
AIOFM ^d	aiofm-1	in-house developed 2D	290-380	0.4	-30	0.2	QDOAS	×	×	PriAM	×	×	-	-	-
NIWA ^e (2)	niwa-30	in-house developed 1D	290-363	0.54	-20	0.5	DOASIS	×	×	-	-	-	-	-	-
CSIC ^f	csic-10	in-house developed 1D	300-500	0.5	-70	0.7	QDOAS	×	-	-	-	-	-	-	-
BSU ^g	bsu-5	in-house developed 1D	300-500	0.4	-40	0.2-1.0	WinDOAS	-	×	-	-	-	-	-	-
AMOIAP ^h	amoiap-2	in-house developed 1D	315-385	0.4	-40	0.3	Andor Solis & in-house developed software	-	×	-	-	-	-	-	-
NIWA (1)	niwa-29	EnviMes 1D	305-460	0.6	20	0.5	DOASIS	×	×	-	-	-	-	-	-
DLR ⁱ (1)	dlrustc-13	EnviMes 1D	300-460	0.6	20	0.4	DOASIS	×	×	-	-	-	-	-	-
DLR (2)	dlrustc-14	EnviMes 1D	300-460	0.6	20	0.4	DOASIS	×	×	-	-	-	-	-	-
USTC ^j (1)	dlrustc-13	EnviMes 1D	300-460	0.6	20	0.4	DOASIS	×	×	HEIPRO	×	×	×	×	-
USTC (2)	dlrustc-14	EnviMes 1D	300-460	0.6	20	0.4	DOASIS	×	×	HEIPRO	×	×	×	×	-
LMU ^k	lmumim-35	EnviMes 2D	300-460	0.6	20	0.4	QDOAS	×	-	M ³	×	-	-	-	-
CMA ^l	cma-7	Hoffmann GmbH 1D	300-450	0.7	Room T	0.8	WinDOAS	×	×	PriAM	×	×	-	-	-
AUTH ^m	-	-	-	-	-	-	-	-	-	BePro	-	-	×	×	×
INTA ⁿ	-	-	-	-	-	-	-	-	-	BePro	-	-	-	-	×

* reference: More details of the instruments are described in Table 2 in Kreher et al., 2019.

- 1225 a. Royal Belgian Institute for Space Aeronomy, Belgium
 b. Department of Chemistry and Biochemistry, University of Colorado, USA
 c. Max Planck Institute for Chemistry, Germany
 d. Anhui Institute of Optics and Fine Mechanics, Chinese Academy of Sciences, China
 e. National Institute of Water and Atmospheric Research, New Zealand
- 1230 f. Spanish National Research Council, Spain
 g. National Ozone Monitoring Research and Education Center BSU (NOMREC BSU), Belarusian State University, Belarus
 h. A. M. Obukhov Institute of Atmospheric Physics, Russia



- i. Deutsches Zentrum für Luft- und Raumfahrt, Germany
- j. School of Earth and Space Sciences, University of Science and Technology of China, China
- 1235 k. Meteorologisches Institut, Ludwig-Maximilians-Universität München, Germany
- l. Chinese Academy of Meteorology Science, China Meteorological Administration, China
- m. Laboratory of Atmospheric Physics, Aristotle University of Thessaloniki, Greece
- n. National Institute of Aerospace Technology, Spain

1240 Table 2 Baseline DOAS analysis settings for the HONO fit.

Parameter	common setting
Fitting spectral range	335-373 nm
Wavelength calibration	Calibration based on Fraunhofer lines of Kurucz solar spectrum (Kurucz et al., 1984)
Cross sections	
HONO	Stutz et al. (2000), 296 K Vandaele et al. (1998), 220 K and 298 K, I_0 -corrected* (10^{17} molecules cm^{-2})
NO ₂	Taylor terms (see Pukite et al. 2010) with respect to σ_{NO_2} at 298 K : $\lambda\sigma_{NO_2}, \sigma_{NO_2}^2$
O ₃	Bogumil et al., (2003), 223 K and 243 K, I_0 -corrected* (10^{20} molecules cm^{-2})
BrO	Fleischmann et al. (2004), 223 K
O ₄	Thalman and Volkamer (2013), 293 K
HCHO	Meller and Moortgat (2000), 297 K
H ₂ O (vapor)	Polyansky et al. (2016) scaled by 2.6 (Lampel et al., 2017)
Ring effect	Ring spectrum calculated based on Kurucz solar atlas and Ring scaled with $(\lambda/354 \text{ nm})^4$ (Wagner et al., 2009)
Intensity offset	Polynomial of order 1 (corresponding to 2 coefficients)
Polynomial term	Polynomial of order 5 (corresponding to 6 coefficients)
Wavelength adjustment	All spectra are shifted and stretched against FRS
Fraunhofer Reference Spectrum (FRS)	1. daily noon FRS (at 11:30) 2. sequential FRS

* solar I_0 correction, Aliwell et al., 2002



Table 3 Common settings of the HONO profile retrievals:

Parameter	Values
Atmosphere definition	pressure, temperature, total air density, and O ₃ vertical profiles averaged from sonde measurements in De Bilt (09/2013-2015); Surface albedo should be fixed to 0.06.
Retrieval altitude grid	0-4 km and step of 200 m. The surface height and instrument altitude are fixed to 0 m.
Wavelength	355nm (effective center of the wavelength range (335-373nm) of the HONO delta SCD retrieval)
Aerosol properties	The single scattering albedo should be fixed to 0.92 and the asymmetry factor to 0.68. The aerosol profiles retrieved at 360nm from O ₄ can be directly used.
Elevation angles	Those used in the measurement acquisition protocol: 1, 2, 3, 4, 5, 6, 8, 15, 30°
Measurement uncertainty covariance	Square of 100% of the SCD fit error for the diagonal terms and extra-diagonal terms are zero.
A priori profiles	Exponentially-decreasing profile derived using the VCD of 3×10^{14} molecules cm ⁻² and a scaling height (SH) value of 0.1km
A priori covariance matrices (Sa)	Square of 100% of the a priori profile for the diagonal terms and extra-diagonal terms are added as Gaussian functions with a correlation length of 200m

Table 4 LP-DOAS Analysis settings.

Parameter	Common setting
Fit range	292.23 – 367.51 nm
NO ₂	Burrows et al., 1998
O ₃	Serdyuchenko et al., 2014
HCHO	Meller and Moortgat (2000), 297 K
HONO	Stutz et al. (2000), 296 K
O ₄	Thalman and Volkamer (2013), 293 K
Lamp spectrum	From measurements
Background spectrum	From measurements
Polynomial	Degree 3